

Martian time-series unraveled: A multi-scale nested approach with factorial variational autoencoders

Ali Siahkoochi, Rudy Morel, Randall Balestrieri, Erwan Allys, Grégory Sainton, Taichi Kawamura,
and Maarten V. de Hoop

Abstract—Unsupervised source separation involves unraveling an unknown set of source signals recorded through a mixing operator, with limited prior knowledge about the sources, and only access to a dataset of signal mixtures. This problem is inherently ill-posed and is further challenged by the variety of timescales exhibited by sources in time series data from planetary space missions. As such, a systematic multi-scale unsupervised approach is needed to identify and separate sources at different timescales. Existing methods typically rely on a preselected window size that determines their operating timescale, limiting their capacity to handle multi-scale sources. To address this issue, we propose an unsupervised multi-scale clustering and source separation framework by leveraging wavelet scattering spectra that provide a low-dimensional representation of stochastic processes, capable of distinguishing between different non-Gaussian stochastic processes. Nested within this representation space, we develop a factorial variational autoencoder that is trained to probabilistically cluster sources at different timescales. To perform source separation, we use samples from clusters at multiple timescales obtained via the factorial variational autoencoder as prior information and formulate an optimization problem in the wavelet scattering spectra representation space. When applied to the entire seismic dataset recorded during the NASA InSight mission on Mars, containing sources varying greatly in timescale, our approach disentangles such different sources, e.g., minute-long transient one-sided pulses (known as “glitches”) and structured ambient noises resulting from atmospheric activities that typically last for tens of minutes, and provides an opportunity to conduct further investigations into the isolated sources.

Index Terms—unsupervised learning, clustering, source separation, multi-scale, variational autoencoders.

I. INTRODUCTION

SOURCE separation involves the often ill-posed problem of retrieving an *a priori* unknown number of source signals from an observed signal, often in the form of a time series. In order to tackle the ambiguity in retrieving the source signals,

Ali Siahkoochi and Maarten V. de Hoop are with the Department of Computational Applied Mathematics and Operations Research, Rice University, Houston, TX 77005, USA (e-mail: alisk@rice.edu; mdehoop@rice.edu).

Rudy Morel is with the Center for Computational Mathematics, Flatiron Institute, New York, NY 10010, USA (e-mail: rmorel@flatironinstitute.org).

Randall Balestrieri is an independent researcher, New York, NY 10010, USA (e-mail: randallbalestrieri@gmail.com).

Erwan Allys is with the Laboratoire de Physique, École Normale Supérieure, Paris, France (e-mail: erwan.allys@ens.fr).

Grégory Sainton is jointly affiliated with LERMA, Observatoire de Paris, PSL research Université, CNRS, Sorbonne Université, 75104, Paris, France and Université Paris Cité, Institut de physique du globe de Paris, CNRS, 75005, Paris, France (e-mail: gregory.sainton@obspm.fr).

Taichi Kawamura is with the Université Paris Cité, Institut de physique du globe de Paris, CNRS, 75005, Paris, France (e-mail: kawamura@ipgp.fr).

source separation methods incorporate available prior information about the sources—traditionally, by making assumptions about the regularity of the sources [1], [2], [3], [4], [5], [6], [7], [8], [9], [10], e.g., sparsity or low-rank structure in some transform domain and certain distributional assumptions. While these traditional methods have been extensively studied and are well understood, their underlying regularity assumptions, if not realistic, can introduce bias into the outcome of the source separation process [5], [11]. For example, the eponymous classical independent component analysis (ICA) [12] source separation method and its variations, e.g., nonlinear ICA [13], generally impose assumptions such as non-Gaussianity and stationarity of sources, which makes their application extremely challenging in noisy environments and when dealing with data that we have very little prior knowledge, e.g., when dealing with data obtained from extraterrestrial missions. In fact, most real-world applications of ICA fall back to separating noise from signal [14], [15] as opposed to separating the sources within the signal that is embedded in noise.

In contrast to the conventional methods, data-driven source separation approaches are able to learn the prior information on sources (either implicitly or explicitly) from data. For example, supervised source separation methods [16], [17], [18], [19], [20], [21], [22], [23] aim to separate sources by utilizing labeled training data, comprising pairs of sources and their mixtures. However, in domains with limited expert knowledge, obtaining labeled training data is often challenging, making supervised learning methods unsuitable. Furthermore, the use of synthetic data to artificially generate labels also proves challenging when the signal to be generated is not thoroughly understood. On the other hand, while unsupervised source separation methods can be applied in domains with no access to labeled data [24], [25], [26], [27], [28], [29], [30], [31], [32], [33], [34], they are not well-suited to handle source separation problems where sources exhibit vastly varying timescales. This is partially due to their reliance on preselected window sizes that limits their usage to separating sources that span within the window’s timescale. This limitation can be a critical obstacle in analyzing complex phenomena that involve sources with vastly different timescales.

To address this problem, we present an unsupervised multi-scale clustering and source separation framework that is capable of detecting and separating prominent sources in a dataset of signal mixtures. Our framework consists of the following building blocks (see Fig. 1 for a schematic diagram),

- **Pyramidal scattering spectra.** In light of the multi-scale nature of the sources, we develop our framework

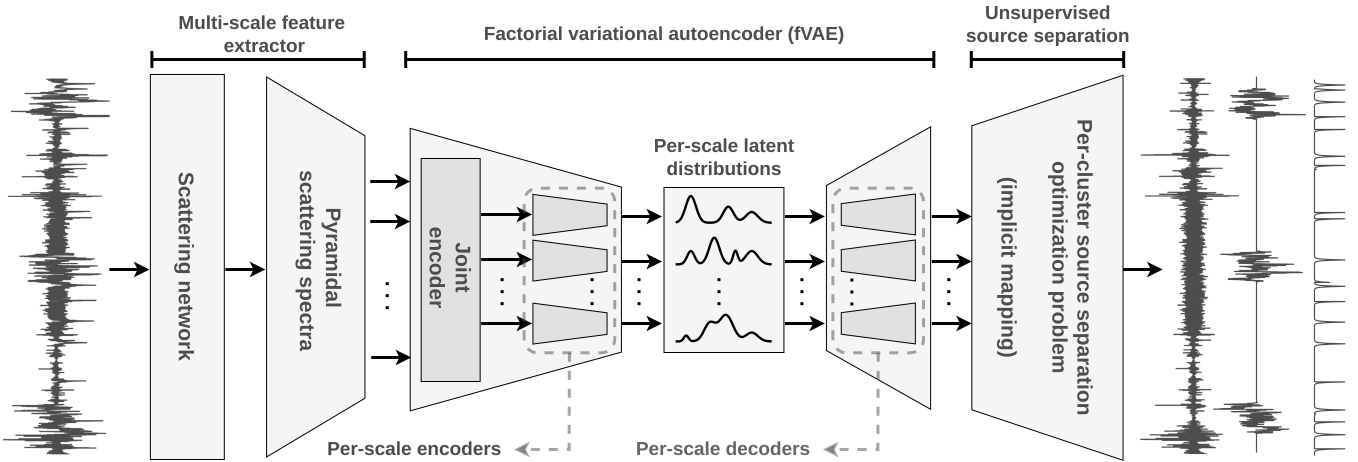


Fig. 1. A schematic diagram depicting the proposed unsupervised multi-scale clustering and source separation framework, consisting of three stages. In the initial stage, indicated on the left in Fig. 1, we convert the data into the pyramidal scattering spectra representation space. The objective of this stage is to represent the data across significantly diverse timescales, ranging from less than a minute to an hour. The second stage involves training a generative model, namely a factorial variational encoder, which learns a joint probabilistic description of the multi-scale representations (indicated in the middle of Fig. 1 with arrows going from one block to another indicating representations associated with different timescales). The goal of this stage is to identify prominent sources in the dataset across several timescales, which will, in turn, be used as “prior information” in source separation. In the final stage, indicated on the right in Fig. 1, we separate the prominent source signals identified by the fVAE in the previous stage via solving an optimization problem in the scattering spectra space with the goal of separating a specific source of interest in the time domain. The code for partially reproducing the results can be found on [GitHub](#).

nested within the wavelet scattering spectra representation space [35]. This multi-scale representation of time series is based on the second moment of scattering network features [36] and is capable of capturing the non-Gaussian and multi-scale characteristics of stationary stochastic processes in the data. To take into account the existence of multiple sources with varying timescales, we propose the pyramidal scattering spectra (first contribution), which involves averaging the wavelet scattering spectra representation at different timescales, resulting in a description of the data that captures non-Gaussian characteristics within different timescales;

- **Factorial variational autoencoder.** Within the pyramidal scattering spectra representation space, we introduce a factorial variant of Gaussian-mixture variational autoencoders (VAEs) [37], [38], [39] (second contribution), hereon referred to as fVAE, that simultaneously learns to probabilistically cluster sources at different timescales—the different factors—in the latent space and independently sample scattering spectra representations associated with each cluster. The former provides clusters of prominent sources in the dataset at different timescales, and the latter models the wavelet scattering spectra distribution of these sources, providing prior information necessary for source separation;
- **Unsupervised source separation.** We perform source separation by complementing the method proposed by [40] by the learned prior information regarding each source (third contribution). Our method for source separation involves solving an optimization problem over

the unknown sources in the wavelet scattering spectra representations space. This is achieved by minimizing carefully selected and normalized loss functions that incorporate prior knowledge about the source of interest, ensure data-fidelity, and promote statistical independence between the recovered sources.

To demonstrate the applicability of our approach, we apply our approach to the full seismic dataset recorded by a seismometer on Mars during NASA’s Interior Exploration using Seismic Investigations, Geodesy and Heat Transport (InSight) mission [41], [42], [43]. The InSight lander’s seismometer—known as the SEIS instrument—detected marsquakes [44], [45], [46], [47] and transient atmospheric signals, such as wind and temperature changes, that provide information about the Martian atmosphere [48] and enable studying the interior structure and composition of the Red Planet [49]. The signal recorded by the InSight seismometer is heavily influenced by atmospheric activity and surface temperature [50], [51]. These non-seismic signals largely vary in timescale from minutes to hours and it would be crucial to capture this in multiple timescale. In addition to providing examples on the seismic dataset recorded during the InSight mission, we demonstrate the results of our approach in a controlled setting when applied to a stylized example involving multi-scale clustering and source separation of time series consisting of sources with three different timescale (cf. Section D of the Appendix).

Through analysis of this complex dataset via our approach, we observe that clusters identified at the finest timescale reveal distinct features such as glitches with and without precursors, with the former showing increased occurrence around Martian

sunset. As the timescale broadens, clusters exhibit longer-duration events like oscillatory signals and bursts of high-frequency energy, possibly associated with wind dynamics. Moreover, coarser timescales unveil phenomena like wind gusts and atmospheric interactions, evident from characteristic waveforms and their occurrence patterns aligned with Martian day-night cycles. By leveraging clusters of glitches and wind-burst noises, we applied our source separation method and successfully separated these sources from the given time series. The results, illustrated through waveform visualizations, indicate successful separation with minimal alterations to the original waveform, validating the effectiveness of the approach. Additionally, as we show in Section C of the Appendix, our method is also capable of separating background noise and glitches from a marsquake, which indicates the applicability of our method in cleaning sources that are not prominent enough to have their own clusters. Finally, the exploration of latent space clusters via the fVAE architecture provides insights into the learned representation of the dataset. Through low-dimensional visualizations, we examined clusters across different timescales. We observed that clusters in finer timescales exhibit clearer boundaries, suggesting more structured data. Moreover, the distribution of quality ‘‘A’’ broadband events and pressure drops across different timescales highlights the multi-scale representation of data captured by the fVAE architecture. Broadband events concentrate more in coarser timescales, while pressure drops are compactly situated in finer timescales, indicating the efficacy of the learned representation in capturing diverse temporal phenomena. Overall, these analyses offer valuable insights into the separation of prominent sources and the structure of latent space clusters, showcasing the capabilities of the proposed methods in analyzing complex datasets.

In the following sections, we introduce the utilization of wavelet scattering spectra as a representation rich in domain knowledge for analyzing multi-scale time series. Furthermore, we explain how we extend this representation to handle non-stationary processes. The core of our approach lies in the description of factorial Gaussian-mixture VAEs, which enable multi-scale probabilistic clustering, which will be used as prior information for source separation. In the final stage of our framework, we detail our source separation approach, which involves solving an optimization problem using loss functions defined in the wavelet scattering spectra space. Lastly, we present the results of applying our approach to the seismic dataset obtained from the InSight mission.

II. PYRAMIDAL SCATTERING SPECTRA

Time-series data \mathbf{x} recorded during space missions are typically non-stationary non-Gaussian noise. Such time-series are multi-scale in two respects. First, the signal \mathbf{x} is a mixture of sources occurring at different timescales, which contributes to its non-stationarity. Second, each individual source has variations on a wide range of scales, which can be observed by looking at a scalogram.

This section constructs a representation adapted to this doubly multi-scale nature of the data by building pyramidal

wavelet scattering spectra. Such representation can be described as a multiple timescales average over diagonal correlation features on a two-layer convolutional neural network with predefined wavelet filters.

A. Wavelet scattering networks

A scattering network [36] is a cascade of wavelet operators \mathbf{W} followed by nonlinear activation function (akin to a typical convolutional neural network). A wavelet transform operator \mathbf{W} is a convolutional operator with predefined wavelet filters that extracts variations at separate scales. These filters include a low-pass filter $\varphi_J(t)$ and J complex-valued band-pass filters $\psi_j(t) = 2^{-j}\psi(2^{-j}t)$, $1 \leq j \leq J$, which are obtained by the dilation of a mother wavelet $\psi(t)$ that have zero mean and a fast decay away from $t = 0$. The wavelet coefficient $\mathbf{W}\mathbf{x}(t, j) = x \star \psi_j(t)$ extracts variations of the input signal $\mathbf{x}(t)$ around time t at scale 2^j . In order to characterize time-evolution of the wavelet coefficients e.g., envelope modulation, we apply a modulus $|\cdot|$ and cascade a second wavelet operator. The output of a two-layer scattering network S is $S(\mathbf{x}) := (\mathbf{W}\mathbf{x}, \mathbf{W}|\mathbf{W}\mathbf{x}|)^\top$, it extracts variations of signal \mathbf{x} and its multi-scale envelopes $|\mathbf{W}\mathbf{x}|$ at different times and different scales. Even though these networks have been successfully employed in tasks such as intermittency analysis [52], clustering [53], event detection and segmentation [54] (with learnable wavelets), they are not sufficient to build an accurate description of a multi-scale process, as they fail to capture crucial dependencies across different scales [35].

B. Capturing non-Gaussian properties through scale dependencies

Sources \mathbf{x} encountered in time-series studied in this paper can be considered are very often non-Gaussian processes. For sake of simplicity, let us assume \mathbf{x} is a stationary source. If \mathbf{x} were Gaussian then the different scale channels of a scattering network would be independent, however it is not the case in practice and these dependencies were shown to be crucial to characterize the non-Gaussian stochastic structure of \mathbf{x} [35]. Such dependencies can be captured by considering the correlation matrix $\mathbb{E}[S(\mathbf{x})S(\mathbf{x})^\top]$:

$$\mathbb{E} \begin{bmatrix} \mathbf{W}\mathbf{x}(\mathbf{W}\mathbf{x})^\top & \mathbf{W}\mathbf{x}(\mathbf{W}|\mathbf{W}\mathbf{x}|)^\top \\ \mathbf{W}|\mathbf{W}\mathbf{x}|(\mathbf{W}\mathbf{x})^\top & \mathbf{W}|\mathbf{W}\mathbf{x}|(\mathbf{W}|\mathbf{W}\mathbf{x}|)^\top \end{bmatrix}. \quad (1)$$

This matrix contains three types of coefficients. Correlation coefficients $\mathbb{E}[\mathbf{W}\mathbf{x}(\mathbf{W}\mathbf{x})^\top]$ come down to the wavelet power spectrum, which characterizes in particular the *roughness* of the signal. Correlation coefficients $\mathbb{E}[\mathbf{W}\mathbf{x}(\mathbf{W}|\mathbf{W}\mathbf{x}|)^\top]$ capture signed interaction between wavelet coefficients. In particular, they detect sign-asymmetry and time-asymmetry in \mathbf{x} [35]. Finally, coefficients $\mathbb{E}\{\mathbf{W}|\mathbf{W}\mathbf{x}|(\mathbf{W}|\mathbf{W}\mathbf{x}|)^\top\}$ capture correlations between signal envelopes $|\mathbf{W}\mathbf{x}|$ at different scales. These correlations account for intermittency and envelope time-asymmetry [35].

Owing to the compression properties of wavelet operators [55] for the type of signals considered in this paper, these matrices are quasi-diagonal. We denote $\mathbb{E}[\text{diag}(S(\mathbf{x})S(\mathbf{x})^\top)]$

an appropriate diagonal approximation of the full sparse matrix in (1). The expectation \mathbb{E} is replaced by a time average denoted by Ave (average pooling) whose size should be chosen as the typical duration of event \mathbf{x} . The wavelet scattering spectra representation is

$$\Psi(\mathbf{x}) := \text{Ave} (S(\mathbf{x}), \text{diag} (S(\mathbf{x})S(\mathbf{x})^\top)). \quad (2)$$

This representation extracts average and correlation features on a two-layer convolutional neural network with predefined wavelet filters. They are analogous to the features extracted in [56] for generation. However, we do not train any weights in our representation. Owing to the compression properties of wavelet operators we obtain a low-dimensional representation. For a signal $\mathbf{x} \in \mathbb{R}^L$ of length L the scattering spectra contain approximately $\log_2^3(L)/6$ coefficients [35]. As a consequence, our representation, composed of order 1 and order 2 moments, can be estimated with low-variance, which can be crucial for clustering and disentangling sources. One can also consider scattering cross-spectra between two signals, \mathbf{x} and \mathbf{y} , defined by $\Psi(\mathbf{x}, \mathbf{y}) = \text{Ave} \text{diag} (S(\mathbf{x})S(\mathbf{y})^\top)$. They capture nonlinear, non-Gaussian dependencies between signals \mathbf{x} and \mathbf{y} .

C. Pyramidal averaging

Non-stationarity in the data \mathbf{x} is in part explained by the presence of sources at different timescales. Our representation $\Psi(\mathbf{x})$ averages scattering spectra features on a certain window. If a source has a time-duration that is much smaller than the average window size, it will be averaged out, and the representation will contain little information about such a source. To take into account the variety of source timescales, we consider different averaging sizes in a causal manner. We replace Ave in (2) by a multi-scale average pooling operator $\text{Ave} = (\text{Ave}_{t \in w_1}, \dots, \text{Ave}_{t \in w_K})$. The windows $w_1 \subset \dots \subset w_K$ have a pyramidal structure, they are of increasing size, and all ending at the same time, where $\text{Ave}_{t \in w_1}$ considers recent past while $\text{Ave}_{t \in w_K}$ considers distant past. To cover a large range of timescales, we choose w_{k+1} to be four times longer than w_k . This defines a *pyramidal scattering spectra* representation $\Psi(x) = (\Psi_1(x), \dots, \Psi_K(x))$ whose factor k is $\Psi_k(\mathbf{x}) := \text{Ave}_{t \in w_k} (S(\mathbf{x}), \text{diag} (S(\mathbf{x})S(\mathbf{x})^\top))$. The representation $\Psi(\mathbf{x})$ decomposes the variation in the stochastic structure of process \mathbf{x} over time, through a multi-scale operator Ave.

III. FACTORIAL GAUSSIAN-MIXTURE VARIATIONAL AUTOENCODER (FVAE)

To perform source separation on our multi-scale representation, we require a generative model that can simultaneously cluster and sample. As Gaussian-mixture VAEs [37], [38], [39] are capable of learning highly structured, low-dimensional latent representations of data, they are a promising candidate for achieving our goals. The major open question remains on the structure of the mapping between the input space time-series and latent space cluster variables. As our aim is to cluster—or separate—sources co-occurring with different timescales, we propose a factorial variant to Gaussian-mixture VAEs to (i) jointly encode the wavelet scattering

spectra representations of different timescales; (ii) learn a low-dimensional Gaussian mixture latent variable for each timescale, enabling clustering; and (iii) independently decode the latent representations of each timescale to be used as prior information in source separation. In the next few subsections we describe our proposed generative model.

A. Generative model

Denote $\mathbf{u} := (\mathbf{u}_0, \dots, \mathbf{u}_{s-1})$ as the pyramidal wavelet scattering spectra representation of an input signal for s scales. Our goal is to approximate the target joint distribution $p(\mathbf{u})$ using variational inference (VI) [57], [58], leveraging samples from this distribution as training data. We achieve this by defining the following generative model,

$$p_\theta(\mathbf{u}, \mathbf{y}, \mathbf{z}) = p_\theta(\mathbf{u} | \mathbf{z})p_\theta(\mathbf{z} | \mathbf{y})p_\theta(\mathbf{y}) \quad (3a)$$

$$= \prod_{i=0}^{s-1} p_\theta(\mathbf{u}_i | \mathbf{z}_i)p_\theta(\mathbf{z}_i | y_i)p_\theta(y_i). \quad (3b)$$

In this expression, \mathbf{z}_i and y_i for $i = 0, \dots, s-1$ represent the Gaussian mixture and categorical latent variables for the i^{th} timescale, respectively. Furthermore, $\mathbf{z} := (\mathbf{z}_0, \dots, \mathbf{z}_{s-1})$ and $\mathbf{y} := (y_0, \dots, y_{s-1})$ represent the collection of latent variables for all timescales. We choose the following parametric distributions for these random variables for all timescales $i = 0, \dots, s-1$,

$$p_\theta(y_i) = \text{Cat}(c_i^{-1} \mathbf{1}_{c_i}), \quad (4a)$$

$$p_\theta(\mathbf{z}_i | y_i) = \mathcal{N}(\mathbf{z}_i | \boldsymbol{\mu}_{z,i}(y_i; \boldsymbol{\theta}), \text{diag}(\boldsymbol{\sigma}_{z,i}^2(y_i; \boldsymbol{\theta}))), \quad (4b)$$

$$p_\theta(\mathbf{u}_i | \mathbf{z}_i) = \mathcal{N}(\mathbf{u}_i | \boldsymbol{\mu}_{u,i}(\mathbf{z}_i; \boldsymbol{\theta}), \text{diag}(\boldsymbol{\sigma}_{u,i}^2(\mathbf{z}_i; \boldsymbol{\theta}))), \quad (4c)$$

where c_i represents the number of components in the Gaussian mixture latent distribution. $p_\theta(\mathbf{z}_i | y_i)$ is modeled as a Gaussian distribution with $\boldsymbol{\mu}_{z,i}(y_i; \boldsymbol{\theta})$ and $\boldsymbol{\sigma}_{z,i}(y_i; \boldsymbol{\theta})$ simply being learnable vectors for each $y_i \in \{0, \dots, c_i - 1\}$, which amounts to a Gaussian mixture model for \mathbf{z}_i . Conditioned on \mathbf{z}_i , \mathbf{u}_i is also modeled as a Gaussian distribution with mean $\boldsymbol{\mu}_{u,i}(\mathbf{z}_i; \boldsymbol{\theta})$ and diagonal covariance $\boldsymbol{\sigma}_{u,i}(\mathbf{z}_i; \boldsymbol{\theta})$ parameterized using deep nets. The generative model setup outlined above translates to having independent decoders—i.e., mappings from latent variables to scattering spectra representations—for each timescale. This approach enables the independent synthesis of scattering spectra representations for each timescale for the downstream source separation step. To train this generative model tractably using VI, we define an inference model in the next section that approximates the latent posterior distribution.

B. Inference model

Evaluating the likelihood of the parametric distribution $p_\theta(\mathbf{u})$ requires marginalizing out the Gaussian mixture and the categorical latent variables from the joint distribution in (3). Unfortunately, this process is computationally infeasible due to the high-dimensionality of these distributions. To overcome this obstacle, we utilize amortized VI to approximate the latent posterior distribution $q(\mathbf{y}, \mathbf{z} | \mathbf{u})$. This approximation uses the Evidence Lower Bound (ELBO) [37], [58] to approximate the model likelihood conditioned on the latent posterior on the

wavelet scattering spectra representations for all timescales. To enable multi-scale clustering of the input data, we employ the following factorization of the posterior distribution,

$$q_\phi(\mathbf{z}, \mathbf{y} | \mathbf{u}) = q_\phi(\mathbf{z} | \mathbf{y}, \mathbf{u})q_\phi(\mathbf{y} | \mathbf{u}) \quad (5a)$$

$$= \prod_{i=1}^s q_\phi(\mathbf{z}_i | y_i, \mathbf{u})q_\phi(y_i | \mathbf{u}). \quad (5b)$$

In the above expression, the pyramidal scattering spectra representation is used to infer the per-scale cluster, which in turn determines the per-scale, per-cluster Gaussian latent distribution (associated component in the Gaussian mixture model). We use the following parameterizations to learn an amortized latent posterior model for each timescale $i = 0, \dots, s-1$,

$$q_\phi(y_i | \mathbf{u}) = \text{Cat}(\boldsymbol{\pi}_i(\mathbf{u}; \phi)), \quad (6a)$$

$$q_\phi(\mathbf{z}_i | y_i, \mathbf{u}) = \mathcal{N}(\mathbf{z}_i | \boldsymbol{\mu}_{z,i}(\mathbf{u}, y_i; \phi), \quad (6b)$$

$$\text{diag}(\boldsymbol{\sigma}_{z,i}^2(\mathbf{u}, y_i; \phi))), \quad (6c)$$

where $\boldsymbol{\pi}_i(\mathbf{u}; \phi)$, parameterized by a neural network, represents the cluster membership probabilities for pyramidal scattering spectra input \mathbf{u} at the i^{th} timescale. Since the inferred latent variable encodes information regarding the cluster membership of \mathbf{u} , we explicitly input both \mathbf{u} and y_i to the neural network parameterizations of the mean $\boldsymbol{\mu}_{z,i}(\mathbf{u}, y_i; \phi)$ and diagonal covariance $\boldsymbol{\sigma}_{z,i}^2(\mathbf{u}, y_i; \phi)$. With the generative and inference models defined, we derive the objective function for training the fVAE in the next section.

C. Training objective function

Training the fVAE involves minimizing the reverse Kullback-Leibler (KL) divergence between the parameterized and true joint distribution,

$$\mathbb{KL}(p(\mathbf{u}) || p_\theta(\mathbf{u})) = \mathbb{E}_{\mathbf{u} \sim p(\mathbf{u})} \left[\underbrace{\log p(\mathbf{u})}_{\text{const. w.r.t. } \theta} - \log p_\theta(\mathbf{u}) \right] \quad (7a)$$

$$= \mathbb{E}_{\mathbf{u} \sim p(\mathbf{u})}. \quad (7b)$$

Evaluating the likelihood $p_\theta(\mathbf{u})$ is intractable due to the required marginalization over \mathbf{y} and \mathbf{z} (cf. (3)). As a result, we approximate the likelihood with ELBO, which amounts to computing the expectation of joint distribution in (3) with respect to the latent posterior distribution, leading to the following training optimization problem:

$$\min_{\theta} \mathbb{E}_{\mathbf{u} \sim p(\mathbf{u})} [-\log p_\theta(\mathbf{u})] \quad (8a)$$

$$\leq \min_{\theta, \phi} \mathbb{E}_{\mathbf{u} \sim p(\mathbf{u})} \mathbb{E}_{\mathbf{z}, \mathbf{y} \sim q_\phi(\mathbf{z}, \mathbf{y} | \mathbf{u})} \left[-\log \frac{p_\theta(\mathbf{u}, \mathbf{y}, \mathbf{z})}{q_\phi(\mathbf{z}, \mathbf{y} | \mathbf{u})} \right] \quad (8b)$$

$$= \min_{\theta, \phi} \sum_{i=1}^s \mathbb{E}_{\mathbf{u} \sim p(\mathbf{u})} \left[\mathbb{E}_{\mathbf{z}_i \sim q_\phi(\mathbf{z}_i | y_i, \mathbf{u})} \underbrace{\left[-\log p_\theta(\mathbf{u}_i | \mathbf{z}_i) \right]}_{\text{Per-scale reconstruction loss}} \right] \quad (8c)$$

$$+ \underbrace{\mathbb{KL}(q_\phi(y_i | \mathbf{u}) || p_\theta(y_i))}_{\text{Categorical prior on } y_i} \quad (8d)$$

$$+ \mathbb{E}_{y_i \sim q_\phi(y_i | \mathbf{u})} \left[\underbrace{\mathbb{KL}(q_\phi(\mathbf{z}_i | y_i, \mathbf{u}) || p_\theta(\mathbf{z}_i | y_i))}_{\text{Gaussian mixture prior on } \mathbf{z}_i} \right]. \quad (8e)$$

The expectations in the optimization problem above can be approximated using Monte Carlo integration over samples from their respective distributions.

IV. UNSUPERVISED SOURCE SEPARATION

In this section, we aim to perform the source separation in the time domain, while the previous section focused on the scattering spectra space. We introduce an unsupervised source separation algorithm based on an optimization problem in the time domain, with a loss function defined in the scattering spectra space. The pretrained fVAE provides a model for the distribution of sources in the scattering spectra space. We use this as prior information in our optimization problem. Combining these techniques allows for identifying and separating unknown multi-scale sources within a given time window, which aligns with the objectives of unsupervised source separation. This approach was initially introduced by [59], [60] and recently adapted to single timescale unsupervised source separation by [40].

Denote \mathbf{x} as a given time window, which is the sum of unknown independent sources s_i , where $i = 1, \dots, M$, possibly occurring at different timescales, with measurement noise $\boldsymbol{\nu}(t)$, so that $\mathbf{x}(t) = \sum_{i=1}^M s_i(t) + \boldsymbol{\nu}(t)$, where $\mathbf{n}(t) = \boldsymbol{\nu}(t) + \sum_{i=2}^M s_i(t)$. Our approach to source separation involves detecting the prominent sources in $\mathbf{x}(t)$ and separating them one-by-one. We assume that the source $s_1(t)$ is associated to one of the clusters identified by our fVAE model and we wish to separate s_1 from the mixture. To address this ill-posed problem, we incorporate prior knowledge in the form of realizations $\{s_1^i\}_{i=1}^N$, which the fVAE identifies as samples from the same cluster as the unknown source. Using these samples, we define three loss terms to ensure that the reconstructed source \tilde{s}_1 has statistics consistent with the collected samples s_1^i , as well as that $\mathbf{x} - \tilde{s}_1$ has the same statistics as \mathbf{n} . It also promotes statistical independence between s_1 and $\mathbf{x} - \tilde{s}_1$. These loss terms are:

$$\mathcal{L}_{\text{prior}}(s_1) = \sum_{i=1}^N \frac{\|\Psi_k(s_1) - \Psi_k(s_1^i)\|_2^2}{\sigma^2(\Psi_k(s_1^i))}, \quad (9a)$$

$$\mathcal{L}_{\text{cross}}(s_1) = \sum_{i=1}^N \frac{\|\Psi_k(s_1^i, \mathbf{x} - s_1)\|_2^2}{\sigma^2(\Psi_k(s_1^i, \mathbf{x}))}, \quad (9b)$$

$$\mathcal{L}_{\text{data}}(s_1) = \sum_{i=1}^N \frac{\|\Psi_k(\mathbf{x} - s_1 + s_1^i) - \Psi_k(\mathbf{x})\|_2^2}{\sigma^2(\Psi_k(\mathbf{x} + s_1^i))}. \quad (9c)$$

The loss in (9a) ensures consistency between the statistics of the recovered signal s_1 with the statistics of the observed signals s_1^i . The loss in (9b) ensures that the reconstruction $\mathbf{x} - s_1$ of \mathbf{n} has implicitly the correct statistics by ensuring $\mathbf{n} + s_1^i$ has consistent statistics with \mathbf{x} . Finally, the loss in (9c) promotes statistical independence between the recovered source s_1 and the recovered noise \mathbf{n} . To facilitate the optimization and to avoid having to choose weighting parameters, each loss term is normalized with respect to the standard deviation of each coefficient in Ψ_k . In this manner, $\sigma^2(\Psi_k(s_1^i))$ represents the vector of variances for each coefficient in Ψ_k computed across

different realizations \mathbf{s}_1^i . The same applies to $\sigma^2(\Psi_k(\mathbf{x} + \mathbf{s}_1^i))$ and $\sigma^2(\Psi_k(\mathbf{s}_1^i, \mathbf{x}))$. We then sum the normalized loss terms to define the reconstruction $\tilde{\mathbf{s}}_1$ as the solution to the optimization problem:

$$\tilde{\mathbf{s}}_1 := \arg \min_{\mathbf{s}_1} [\mathcal{L}_{\text{data}}(\mathbf{s}_1) + \mathcal{L}_{\text{prior}}(\mathbf{s}_1) + \mathcal{L}_{\text{cross}}(\mathbf{s}_1)]. \quad (10)$$

The algorithm relies solely on constraints in the scattering spectra space, except for the initialization $\tilde{\mathbf{s}}_1 = \mathbf{x}$, which contains valuable information about the mixture of sources in the time domain.

V. RESULTS

The purpose of our approach unsupervised multi-scale clustering and source separation framework is to address challenges associated with source separation in domains where limited expert knowledge on the sources is available and source also exhibit vastly different timescales.

We demonstrate the effectiveness of our approach on seismic data recorded by the InSight mission. The data consists of seismic records from the SEIS instrument, which has been operational on Mars since 2018. The dataset contains a variety of signals, including marsquakes, glitches, and wind imprints, each with different timescales. We aim to cluster and separate these sources using our proposed framework. We present the results of our approach in the following subsections. Additional results regarding this experiment are provided in Sections A to C of the Appendix. Finally, we also showcase our approach in a controlled setting through a stylized example that mimics some of the sources observed in the Mars dataset (cf. Section D of the Appendix).

A. Seismic records from the InSight mission

Martian seismic ambient signals consist of signals from various sources, each with different timescales. For instance, at shorter timescales, we expect to observe transient one-sided pulses known as glitches (tens of seconds in duration) [61]. These glitches likely stem from thermal cracks within the instrument’s subsystems or atmospheric phenomena like dust devils—local low-pressure structures moving along the ambient wind (also lasting tens of seconds) [48]. Conversely, at longer timescales, we anticipate observing different phenomena such as regional winds whose direction and speed vary over time. These atmospheric phenomena strongly correlate with temperature, exhibiting a notable dependency on the local time at the station [48].

Moreover, the InSight SEIS instrument—a three-axis instrument (separated by 120°) called U, V, W—has recorded several major marsquakes, which hold significant importance for the insights they offer into the Martian subsurface [62]. However, due to their rarity in comparison to the aforementioned signal types (only 39 events over the course of four years [47]), clustering approaches are not naturally inclined to assign a cluster to marsquake recordings. Nevertheless, as we shall demonstrate, these signals tend to concentrate in the fVAE’s latent space associated with the correct timescale. This concentration serves as an indication of the rich structure of our multi-scale representation of this dataset.

B. Architecture

The architecture of the fVAE primarily relies on fully connected layers. The input consists of concatenated pyramidal wavelet scattering spectra, which are then passed through the joint encoder. This module is composed of a series of fully connected residual blocks, totaling four blocks. Each block includes a fully connected layer that reduces the dimensionality of the concatenated features to a hidden dimension, here set to 1024. This is followed by a Batchnorm layer and LeakyReLU nonlinearity. The output of the residual block is then brought back to the input dimensionality using another fully connected layer, and the result is added to the input (skip connection) to form the output of the residual block. Thanks to the pyramidal scattering spectra representation, the joint encoder with skip connection preserves maximal information from each scale and learns to extract useful information for generative modeling and clustering of representations.

Moving on to the per-scale encoders, the output of the joint encoder is split among different scales, and each scale is fed to a per-scale encoder. These encoders consist of compositions of four fully connected layers, Batchnorm, and LeakyReLU activations. The first layer changes the dimensionality of each scale’s representation to the hidden dimension (1024), while the last layer reduces this hidden dimension to the latent dimension of 32. We parameterize the latent distribution of each scale as a Gaussian mixture model with nine components, where the mean and diagonal covariances are unknown vectors. On the decoding side, the per-scale decoders mirror the per-scale encoders and reconstruct the input multi-scale representation from the latent space.

C. Training details of the factorial variational autoencoder

We utilized the entire data recorded during the InSight mission [63] to train the fVAE. During training, we randomly reserved 10% of the data as validation data for tuning a set of hyperparameters. Following the approach of [64], we employed nine clusters at each timescale (see Section A of the Appendix for a discussion on correspondence with results in [64]). The fVAE was trained using the architecture outlined above, employing a hidden dimension of 1024 and a latent dimension of 32. The Adam optimization algorithm [65] was employed with a learning rate of 10^{-3} . Training was conducted for 1000 epochs, utilizing a batch size of 16384. To address non-differentiability concerns associated with the categorical distribution learning, we utilized the Gumbel-Softmax distribution, enabling a differentiable approximate sampling mechanism for categorical variables [39]. The initial temperature parameter for the Gumbel-Softmax distribution was set to 1.0, and we exponentially decayed the temperature to a minimum value of 0.5. Training takes approximately 51 hours on a Tesla V100. We repeated the training with multiple different random seeds and observed relatively good stability. Specifically, the main clusters are still present in different runs, albeit slight changes to the histogram exist (possibly due to the data points lying on the border of different mixture components). We present the reconstruction quality of the pyramidal scattering spectra by the fVAE in Section B of the Appendix.

D. Identification of clusters across different timescales

To obtain the aforementioned representation, we consider four different timescales to cover the range of timescales that the sources within the dataset of interest might exhibit. We utilize nine-component Gaussian mixture latent variables motivated by a previous study conducted by [64], where the authors provided a single-scale clustering of this dataset using Gaussian mixture models. Since our approach will provide nine clusters per timescale, we expect some of the clusters to be redundant, i.e., share a lot of similarities to one another. Based on existing studies on seismic data from the InSight mission [61], [48], [64], we selected the finest timescale to be 51.2 seconds, which is equivalent to a window size of 4^5 samples with 20 samples per second. This choice allows us to capture the diversity present in the one-sided pulses. To determine the subsequent timescales, we multiplied the previous timescale by a factor of four. While we do not expect to cluster broadband marsquakes [45] due to their infrequent occurrence compared to other sources, we set the largest window size to be 54.6 minutes, i.e., a window size of 4^8 samples. This window size covers marsquakes and other sources related to atmospheric-surface interactions [48].

While further investigation will be necessary to fully uncover the nature of the different clusters detected by our study, the results we obtained already demonstrate that the multi-scale approach successfully distinguishes the various phenomena observed in the Martian data. We provide information on all identified clusters within the four timescales considered in Section A of the Appendix and present the notable clusters in this section. Specifically, Figs. 2 and 3 illustrate two noteworthy identified clusters for the finer (51.2 seconds and 3.4 minutes) and coarser (13.6 minutes and 54.6 minutes) timescales, respectively. To visualize clusters across the four timescales, we depict both the cluster occurrence time histogram along with ten aligned waveforms from that cluster. The cluster occurrence time histogram, i.e., the distribution of windows belonging to that cluster throughout the entire mission, will allow us to identify what times of the day a cluster may exhibit more occurrence, which in turn might reveal clusters that contain atmosphere-surface interaction signals. The aligned waveforms, on the other hand, are useful in identifying the main feature of each cluster. We adopt the approach outlined in [64] to generate the aligned waveforms. This procedure entails calculating, for each cluster within each timescale, the Pearson correlation coefficient between the most probable three component waveform assigned to that cluster (identified via the fVAE) and the remaining three components waveforms in that cluster, adjusted for lag to maximize correlation. Finally, we present the most probable waveform with each component plotted separately, along with nine other aligned waveforms (based on the lag producing the maximum correlation) for the waveforms exhibiting the highest correlation.

a) 51.2-second timescale: At the finest timescale, we identified two clusters where the primary features in both of the clusters are glitches (see Figs. 2a and 2b). The glitches in Fig. 2b contain a precursor, i.e., a high amplitude spike

right before the glitch, and while not being restricted to a time interval during one Martian day, they tend to be observed more frequently close to the sunset. This observation, albeit for glitches in general and not just glitches with precursors, has been independently made in prior work [64], which further confirms the nature of this cluster. Note that while the glitches in Fig. 2b uniformly contain one-sided pulses with increasing amplitude in the U components and decreasing amplitudes in the V and W components, this is due to visualizing aligned waveforms and we do indeed detect other combinations in this cluster. Cluster 6 of this timescale Fig. 2a, however, contains glitches without a precursor, has been detected in almost twice as many windows as cluster 7 (glitches with precursor, Fig. 2b), and has a significant peak around the sunset.

b) 3.4-minute timescale: In this timescale, the main feature of the clusters is often longer in timescale. For example, we obtain a distinct cluster that contains an oscillatory signal with an approximate 25-second period (see Fig. 2c). This cluster appears to mostly occur during Martian night, however, the oscillatory signal might also be present during the day but is drowned in high amounts of ambient daytime noise. No clear root cause for this oscillatory signal has yet been identified, but the analyses carried out show that there is no correlation with the pressure drops, but one has been noted with the wind. For the moment, any instrumental origin seems to have been ruled out. Note that at least two of the aligned waveforms in Fig. 2c also contain glitches, but a closer look reveals the existence of the oscillatory signal. In addition, we identify a cluster that contains one or more bursts of high-frequency, quickly dissipating energy (see Fig. 2d). It is worth noting that due to the high occurrence rate of glitches, the clusters identified in coarser timescales often also include glitches. However, except for the multi-glitch clusters, we argue glitches in coarser timescales are not the main characterizing feature of the clusters according to the aligned waveform plots.

c) 13.6-minute timescale: While in this timescale we still obtain clusters dominated by glitches, we also see clusters associated with surface-atmosphere interactions to emerge. The noteworthy clusters are presented in Figs. 3a and 3b. The cluster in Fig. 3a clearly contains waveforms with a sharp onset and a following ringing oscillations. This feature is observed when a strong wind gust blows. Note that the length of this feature is longer than the high-frequency events with quickly dissipating energy in Fig. 2d. This might suggest that the winds captured in this cluster seem to be sustained longer. Interestingly, the cluster occurrence time histogram of this cluster in Fig. 2d suggests that these winds occur mostly before and after sunset. Another cluster that we observe in this timescale is shown in Fig. 3b. The waveforms associated with this cluster seem to have a distinct “noisy” pulse in the middle, with high-frequency, high-amplitude waveforms before and after it. These might suggest a cluster of dust devils. The occurrence time histogram of this cluster also consistent with the time interval that dust devils are more frequently observed (09:00 to 15:00 LMST), which is confirmed by the InSight mission pressure sensors [66] as well as through the Pathfinder lander [67].

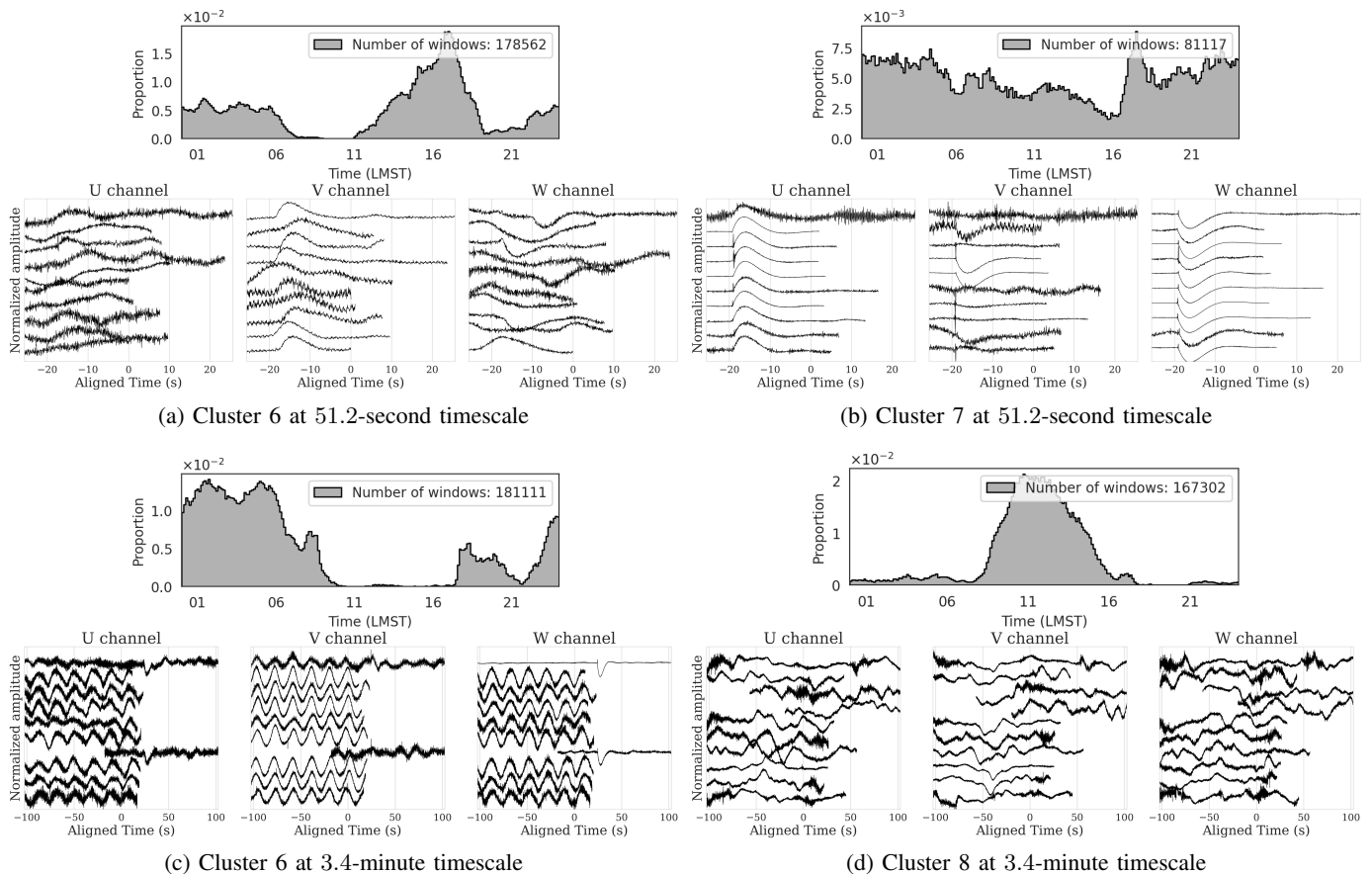


Fig. 2. The visualization of the cluster occurrence time histogram, obtained by aggregating data across the entire mission, and ten aligned waveforms of two clusters belonging to the finer timescales. The horizontal axis on the time histograms represents local mean solar time (LMST). As expected, the finest time scale is capable of distinguishing between two types of glitches: with (Fig. 2a) and without (Fig. 2b) a precursor. According to their occurrence time histogram (horizontal axis on the time histograms is one Martian day), both of these glitch clusters have a tendency to appear more frequently around the Martian sunset. However, the glitch cluster without a precursor, seems to be more localized in time. In the 3.4-minute timescale, clusters are characterized by longer timescales. The cluster in Fig. 2c exhibits an oscillatory signal with an approximate 25-second period, predominantly occurring during Martian night and the cluster in Fig. 2d shows bursts of high-frequency, rapidly dissipating energy.

d) 54.6-minute timescale: When focusing on the largest timescale, we again observe larger scale phenomena that were not captured in fine-scale clusters (recall Fig. 2). Notably, a wind cluster, as depicted in Fig. 3c, exhibits similar characteristic waveforms to the wind cluster in the 13.6-minute timescale Fig. 3a, such as a sharp onset followed by ringing oscillations. However, upon examining the time histograms in Figs. 3a and 3c, it becomes evident that the cluster associated with Fig. 3a indicates a more significant dip after sunset compared to the other. Knowing that the wind speeds consistently decrease to very low levels approximately 2-4 hours after sunset [48], the significant dip in the time histogram of Fig. 3c can be due to the fact that there are fewer 54.6-minute long windows during this period that do not coincide with the low-wind interval compared to the number of 13.6-minute long windows. Finally, the cluster in Fig. 3d contains atmospheric signals related to the sunrise based on the cluster's occurrence time histogram and the gradual increase in

waveform amplitude, which is expected as the ambient noise recorded via the SEIS instrument during the day is consistently higher.

E. Seasonal impacts on surface-atmosphere interactions

To gain deeper insights into atmospheric-surface interactions, we investigate the impact of seasonal changes on the cluster occurrence time histograms. Using the clustered windows from all timescales, we computed occurrence time histograms for each cluster using aggregated data from all four seasons on Mars. We superimposed the per-season occurrence time histograms for all the clusters presented in Figs. 2 and 3, and overlay the per-season average sunrise (solid lines) and sunset (dashed lines) times to facilitate the interpretation of the histograms. Fig. 4 summarizes the results.

Upon visual inspection, we can confirm that the characteristic waveforms for all clusters at different time scales maintained the same structure as illustrated in Figs. 2 and 3.

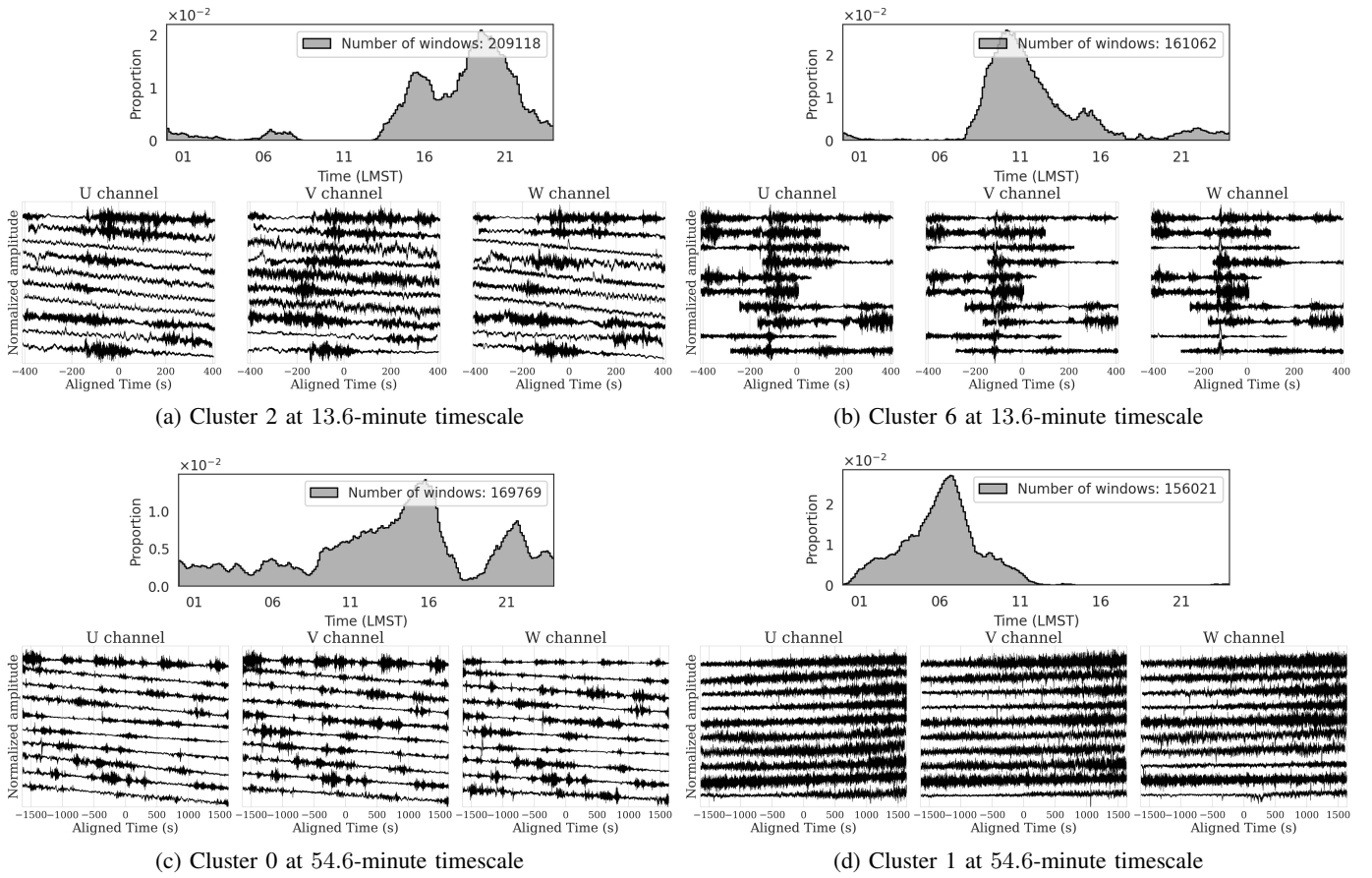


Fig. 3. The visualization of the cluster occurrence time histogram, obtained by aggregating data across the entire mission, and ten aligned waveforms of two clusters belonging to the coarser timescales. The horizontal axis on the time histograms represents local mean solar time (LMST). When focusing on coarser timescales, we start to see events that were not captured in the fine timescale clusters. Notably, Figs. 3a and 3c show some characteristic waveforms with a sharp onset and a following ringing oscillations. Such waveforms are observed when a strong wind gust is blowing. This is also consistent with the occurrence time histogram of these clusters, which are localized in time [48]. Fig. 3d shows a cluster of waveform dominated by sunrise-related surface-atmospheric interactions. This can be inferred based on the cluster’s occurrence time histogram as well as the gradual increase in waveform amplitude, which is related to the higher ambient seismic noise during the Martian daytime.

This ensures the nature of the clusters is unchanged across time, making comparing their histograms relevant. We make the following observations. While we acknowledge that not all variations observed in the time histograms can be solely attributed to seasonal changes (e.g., operational changes of the lander and having access to less data during the winter), we identified that clusters with Martian daytime occurrences exhibited a tendency to shift in their peaks. Furthermore, we also observe that some clusters exhibit slight changes in their distribution, mainly involving a reduction or increase of their peaks. Notable clusters involve the glitch clusters at the finest scale (see Figs. 4a and 4b). Specifically, we can observe that we have detected more waveforms during Martian daytime over the winter and fall seasons, which might be related to less ambient seismic noise due to lower temperatures, allowing our approach to identify more glitches during the day. In addition, as mentioned before, glitches tend to occur more near sunset, which we still can observe from the peak in per-season time histograms with the peak time clearly shifting with the average

sunset time per season.

While we observe strong correlations between the occurrence time histograms and atmospheric conditions, it is worth mentioning that there are seismic signals in each cluster unaffected by seasonal changes. However, the heavy imprint of atmosphere-surface interactions skews the histograms nonetheless. In the next sections, we will indicate that indeed certain seismic events are concentrated in a few clusters, even though they are not the main characterizing feature of those clusters.

F. Unsupervised separation of prominent sources

Given access to clusters of glitches of wind-burst noises, in this section, we show that using samples from these clusters, we can perform source separation using the method described in Section IV. In this method, a particular source of interest can be separated from a given time series provided that we have access to several data snippets that does not contain that source of interest. Here explore separating glitches and the imprint of wind bursts. Figs. 5 and 6 summarizes the results,

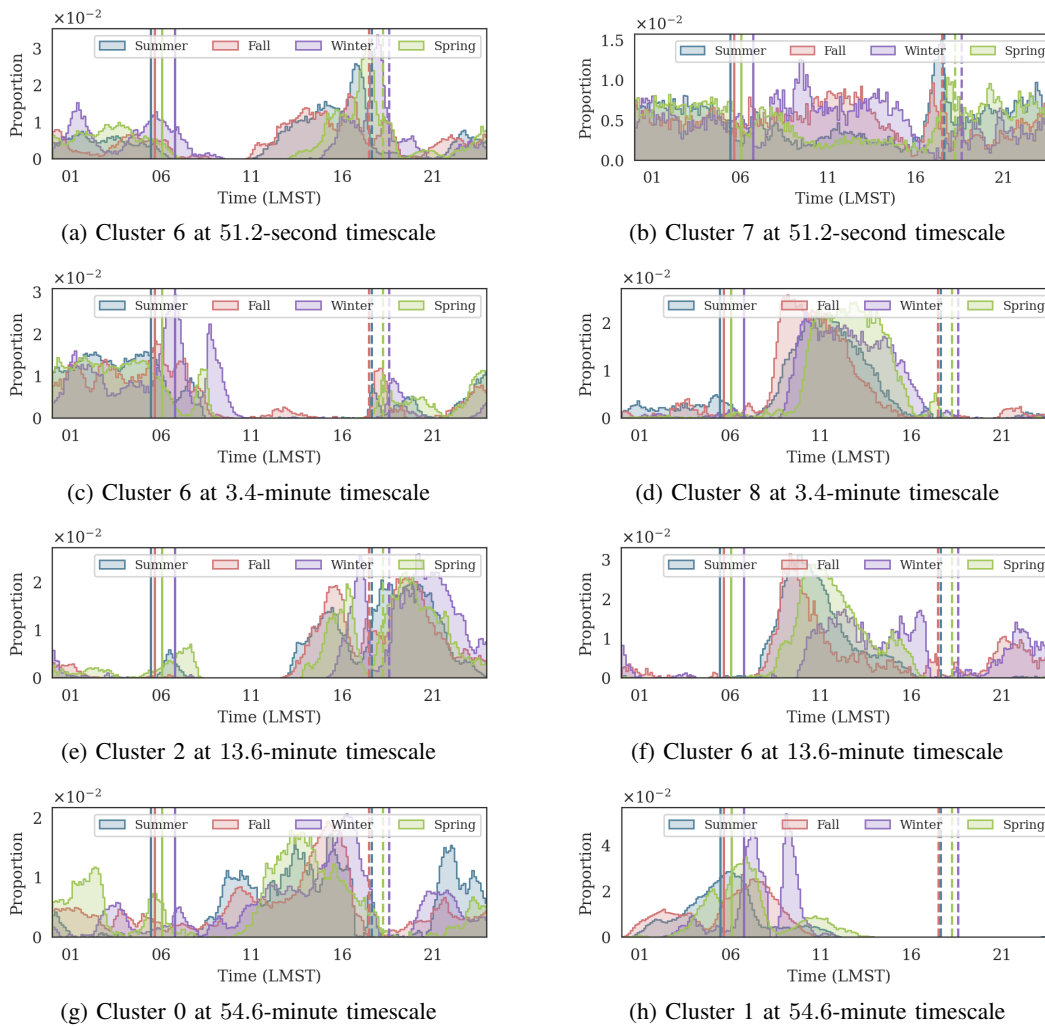


Fig. 4. An overlay of occurrence time histograms of selected clusters within four timescales where time histograms are obtained by aggregating data from Martian local spring (green), summer (blue), fall (red), and winter (purple). The horizontal axis on the time histograms represents local mean solar time (LMST). Each time histogram is associated with the clusters presented in Figs. 2 and 3 where each row represents a distinct timescale, with timescale increasing from top to bottom. The vertical and dashed lines correspond to average sunrise and sunset times over the associated season, respectively. Clusters with Martian daytime occurrences exhibited a tendency to shift in their peaks. Additionally, some clusters exhibit slight changes in their distribution, mainly involving a reduction or increase of their peaks as seasons change.

and we provide details and observations for each experiment below. We also provide an example for separating background noise and glitches from a marsquake (cf. Section C of the Appendix), which extends the application of our method to sources that are less prominent in the dataset.

a) Glitch separation: For the glitch separation experiment, we select a 54.6-minute long waveform during Martian nighttime with several glitches (cf. Fig. 5a). We use 300 samples from cluster 5 in the 51.2-second timescale as its occurrence time histogram mostly concentrated during Martian night and its characteristic waveforms contain no glitches. Figs. 5b and 5c depicts the waveform after separation of glitches and the separated glitches, respectively. The last four rows of Fig. 5 illustrate the zoomed-in views of the results with columns from left to right being raw waveform, waveform after separation of glitches, and the separated glitch,

respectively. These figures indicate the successful separation of glitches as the one-sided pulses are removed with minimal changes to the rest of the waveform. Specifically, the last row of Fig. 5j indicates a zoomed-in view of a portion of the raw waveform that contains no glitches, and our method does not separate any coherent signal from the waveform, which is a crucial property of our method.

b) Wind burst imprint separation: For the wind burst imprint separation we select a Martian daytime 54.6-minute long waveform (cf. Fig. 6a). We use 300 samples from cluster 1 in the 51.2-second timescale as its occurrence time histogram mostly concentrated during Martian day and its characteristic waveforms contain no visible wind bursts. Figs. 6b and 6c depicts the waveform after separation of glitches and the separated glitches, respectively. The last four rows of Fig. 6 illustrate the zoomed-in views of the results with columns from

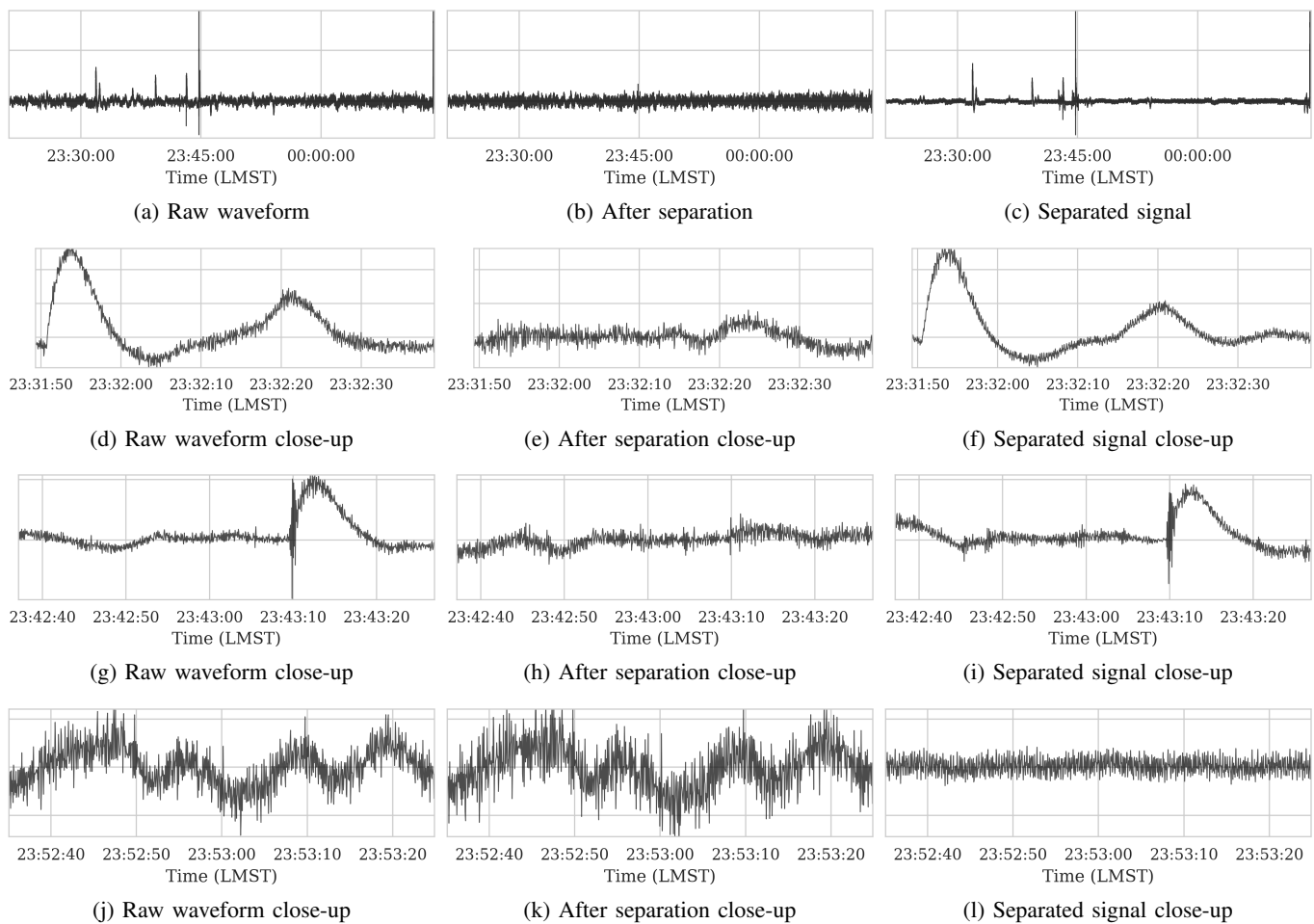


Fig. 5. Separating glitches from a waveform extracted from cluster 4 from the 54.6-minute timescale. The cluster from which the raw waveform is selected is mostly concentrated during the Martian daytime waveform, we select as prior information 300 samples from cluster 5 in the 51.2-second timescale. This cluster has occurrence time histogram mostly concentrated during Martian night and its characteristic waveforms contain no glitches. As such, samples from this cluster would be good candidates for “background” signals that could allow for separating glitches.

left to right being raw waveform, waveform after separation of the wind burst imprint, and the separated wave burst imprint, respectively. These figures indicate the successful separation of wind burst imprints as the wind burst imprint (sharp onset followed by ringing oscillations) is removed with minimal changes to the rest of the waveform.

G. Latent space exploration of clusters

Towards better exploring the learned representation of fVAE, i.e., the per-scale representation obtained after the fVAE encoder, we visualize a low-dimensional representation of the entire dataset. We obtain this low-dimensional representation of the latent space via the UMAP algorithm [68], where we reduce the dimensionality of latent vectors from 32 (see Section V-B for a more detailed description of the architecture) to a two-dimensional representation. We obtain this two-dimensional representation independently for each scale and identify the most likely cluster that each point belongs to (computed through the fVAE) via colors. Fig. 7 contains

these visualizations where each row corresponds to a different timescale with timescales increasing from top to bottom. To illustrate the importance of having a multi-scale representation, we overlay quality “A” broadband events (left column, with black star symbols) and the pressure-drop events for each timescale (right column, with black circles). Note that due to our pyramidal scattering spectra construction mechanism, we have the same total number of latent samples in each scale while the number of samples identified as quality A events or pressure drops increases for larger timescales. Broadband events, i.e., marsquakes, typically have a length of 30–60 minutes and as such, even though we have observed very few of them during the mission and we cannot expect to have a cluster associated with them, we expect a good representation of data to concentrate them in the latent space. Similarly, we expect pressure drops, which have a timescale of less than a minute to be well concentrated in the smaller timescale representations.

We make the following observations. The clusters in the 3.4-minute and 13.6-minute timescales (second and third rows

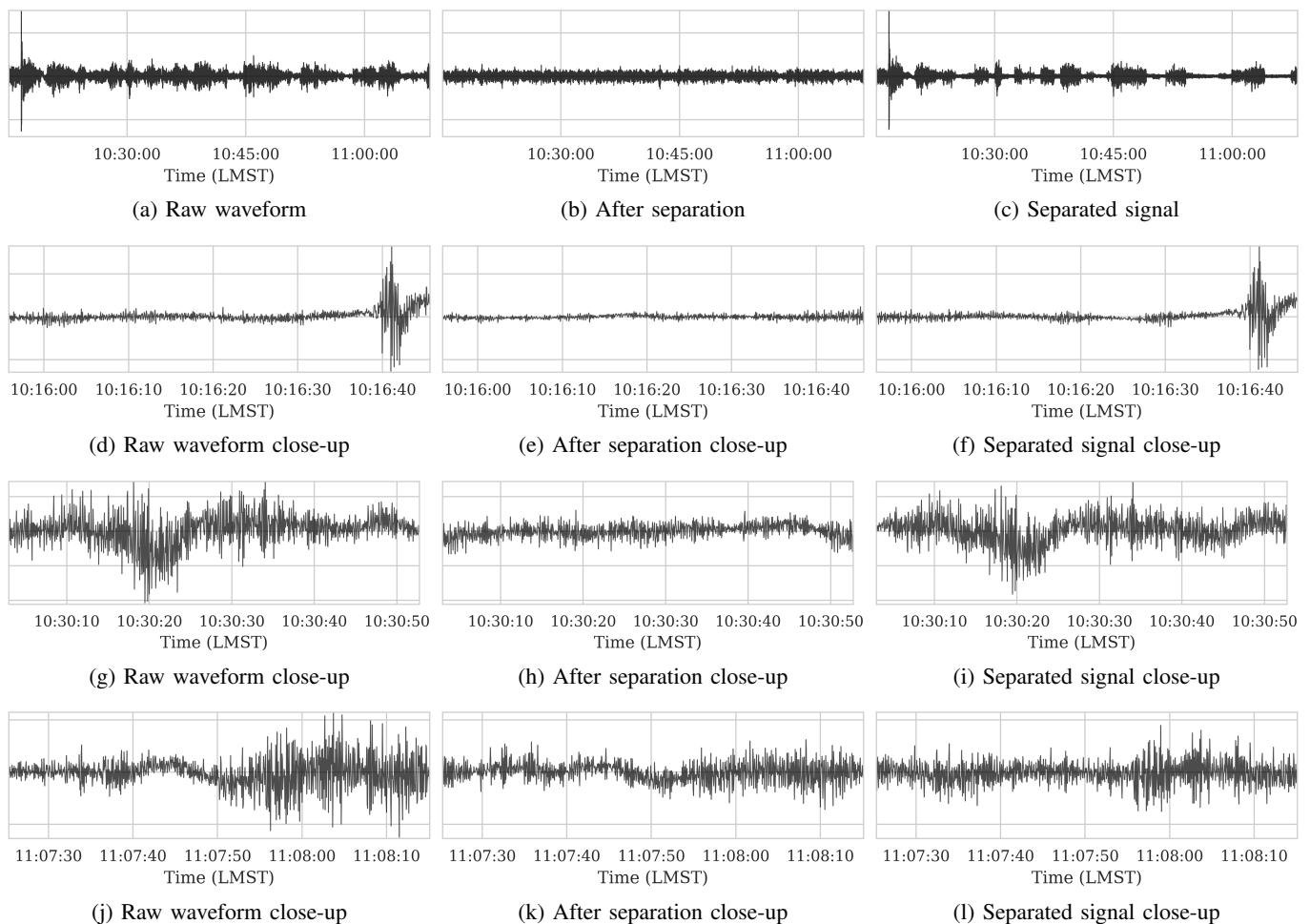


Fig. 6. Separating imprints of the wind from a waveform extracted from cluster 3 from the 54.6-minute timescale. The cluster from which the raw waveform is selected is mostly concentrated during the Martian daytime and in order to remove glitches from this daytime waveform, we select as prior information 300 samples from clusters 1 and 6 in the 51.2-second timescale. These clusters have occurrence time histograms mostly concentrated during the day and their characteristic waveform exhibit no wind burst signatures. As such, samples from these clusters would be good candidates for “backgrounds” signals that could allow for separating wind burst related noises.

of Fig. 7), compared to the finest and coarsest timescales, have clearer boundaries, which suggest that there is more structure in the data in these timescales. The 51.2-second timescale clusters are also relatively well separated, except for the area in the middle of Figs. 7a and 7b that contains mixed samples from several clusters. The 54.6-minute timescale cluster visualization, however, shows less cohesive structures and the points from several clusters are spread throughout the low-dimensional space. This might indicate that there is a less effective number of clusters at this scale. Nonetheless, we importantly observe that the quality “A” broadband events are much more concentrated in the coarsest time scale (see Fig. 7g) compared to the others, with the concentration deteriorating as the timescale decreases. On the other hand, the pressure drops, which have a very short timescale, are very compactly situated in the finest timescale latent space while being spread across multiple clusters in the coarser timescales. These observations regarding the broadband and pressure-

drop events indicate that the learned multi-scale representation appears to be meaningful and to yield localization in the latent space.

VI. DISCUSSION AND CONCLUSION

In order to attain accurate source separation, having prior understanding of the sources is essential. Unsupervised source separation methods offer a solution when expert domain knowledge on the existing source signals is limited by learning to extract sources solely from a dataset of source mixtures. However, when dealing with data containing sources of highly varied timescales, an architecture with appropriate inductive biases is needed to enable multi-scale treatment of source separation. In our work, we propose an approach using factorial variational autoencoders (fVAE) nested within the pyramidal wavelet scattering spectra representation. The intricate treatment of the multi-scale nature of the data—via pyramidal scattering spectra—can be also integrated in other

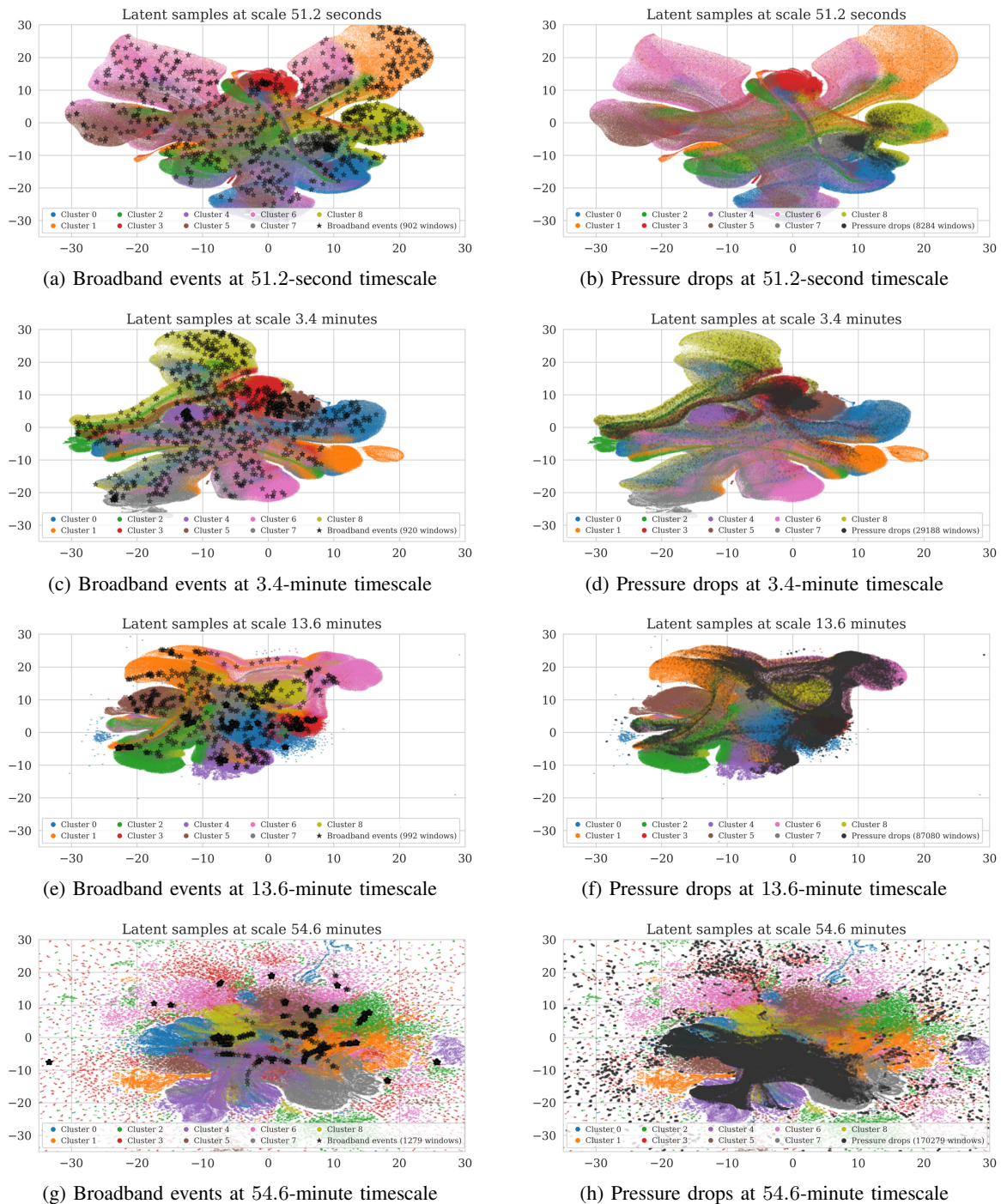


Fig. 7. fVAE latent space low-dimensional visualization, via UMAP [68], across four timescales overlaid with quality “A” broadband events or pressure drops. The left column overlays quality “A” broadband events with star symbols, and the right column indicates pressure drops with black circles. The timescale of the plots increase from top to bottom. Due to our pyramidal scattering spectra construction mechanism, we have the same total number of latent samples in each scale while the number of samples identified as quality A events or pressure drops increases for larger timescales. Nonetheless, we observe broadband events tend to concentrate better in the largest timescale, which corresponds to the timescale typically exhibited by marsquakes. Similarly, pressure drops that are very short in timescale concentrate very well in the shortest timescale.

clustering and source separation methods and its usage is not limited to the proposed fVAE architecture. Our results on data from NASA’s InSight mission demonstrate that the multi-scale fVAE approach successfully identifies different non-seismic phenomena in the InSight data. While small timescale

detect more of the transient signals such as glitches, the large timescale captures more of the global characteristics of the background noise, which is more likely related regional change in atmospheric conditions. The fVAE in turn enables unsupervised source separation by leveraging prior knowledge

from the clusters. This approach makes minimal assumptions about the sources and provides a truly unsupervised method for source separation in non-stationary time-series with multi-scale sources.

Future work involves letting the mother wavelet in the scattering network to be learned, e.g., using [69]. In that setting, the mother wavelet is no longer specified a priori, but is rather parametrized by a few learnable parameters. Those parameters can then be learned to adapt the shape of the mother wavelet—and thus of all the signal statistics that the scattering network computes—to better minimize the loss at hand. Because the parametrization only adds a few parameters, overfitting is not an issue, even in noisy settings, as demonstrated in [53].

REFERENCES

- [1] J.-F. Cardoso, "Source separation using higher order moments," in *International Conference on Acoustics, Speech, and Signal Processing*, vol. 4, 1989, pp. 2109–2112.
- [2] C. Jutten and J. Herault, "Blind separation of sources, part I: An adaptive algorithm based on neuromimetic architecture," *Signal Processing*, vol. 24, no. 1, pp. 1–10, 1991.
- [3] E. Bingham and A. Hyvärinen, "A fast fixed-point algorithm for independent component analysis of complex valued signals," *International Journal of Neural Systems*, vol. 10, no. 01, pp. 1–8, 2000.
- [4] A. Nandi and V. Zarzoso, "Fourth-order cumulant based blind source separation," *IEEE Signal Processing Letters*, vol. 3, no. 12, pp. 312–314, 1996.
- [5] J.-F. Cardoso, "Blind signal separation: Statistical principles," *Proceedings of the IEEE*, vol. 86, no. 10, pp. 2009–2025, 1998.
- [6] C. Jutten, M. Babaie-Zadeh, and S. Hosseini, "Three easy ways for separating nonlinear mixtures?" *Signal Processing*, vol. 84, no. 2, pp. 217–229, 2004.
- [7] L. Zhen, D. Peng, Z. Yi, Y. Xiang, and P. Chen, "Underdetermined blind source separation using sparse coding," *IEEE Transactions on Neural Networks and Learning Systems*, vol. 28, no. 12, pp. 3102–3108, 2017.
- [8] W.-L. Hwang, K.-S. Lu, and J. Ho, "Constrained null space component analysis for semiblind source separation problem," *IEEE Transactions on Neural Networks and Learning Systems*, vol. 29, no. 2, pp. 377–391, 2018.
- [9] Y. Liu, W. Dong, and M. Zhou, "Frame-based variational bayesian learning for independent or dependent source separation," *IEEE Transactions on Neural Networks and Learning Systems*, vol. 29, no. 10, pp. 4983–4996, 2018.
- [10] M. Guzik and K. Kowalczyk, "On ambisonic source separation with spatially informed non-negative tensor factorization," *IEEE/ACM Transactions on Audio, Speech, and Language Processing*, vol. 32, pp. 3238–3255, 2024.
- [11] L. Parra and P. Sajda, "Blind source separation via generalized eigenvalue decomposition," *Journal of Machine Learning Research*, vol. 4, pp. 1261–1269, Dec. 2003.
- [12] T.-W. Lee, *Independent Component Analysis: Theory and Applications*. New York, NY: Springer, 1998.
- [13] A. Hyvärinen and P. Pajunen, "Nonlinear independent component analysis: Existence and uniqueness results," *Neural networks*, vol. 12, no. 3, pp. 429–439, 1999.
- [14] G. Salimi-Khorshidi, G. Douaud, C. F. Beckmann, M. F. Glasser, L. Griffanti, and S. M. Smith, "Automatic denoising of functional mri data: Combining independent component analysis and hierarchical fusion of classifiers," *Neuroimage*, vol. 90, pp. 449–468, 2014.
- [15] P. Hoyer, "Independent component analysis in image denoising," Master's thesis, Helsinki University of Technology, 1999.
- [16] H. Kameoka, L. Li, S. Inoue, and S. Makino, "Supervised determined source separation with multichannel variational autoencoder," *Neural Computation*, vol. 31, no. 9, pp. 1891–1914, 2019.
- [17] D. Wang and J. Chen, "Supervised speech separation based on deep learning: An overview," *IEEE/ACM Transactions on Audio, Speech, and Language Processing*, vol. 26, no. 10, pp. 1702–1726, 2018.
- [18] Y. Luo and J. Yu, "Music source separation with band-split RNN," *IEEE/ACM Transactions on Audio, Speech, and Language Processing*, vol. 31, pp. 1893–1901, 2023.
- [19] X. Zhang, J. Tang, H. Cao, C. Wang, C. Shen, and J. Liu, "Cascaded speech separation denoising and dereverberation using Attention and TCN-WPE networks for speech devices," *IEEE Internet of Things Journal*, vol. 11, no. 10, pp. 18 047–18 058, 2024.
- [20] Y. Özer and M. Müller, "Source separation of piano concertos using musically motivated augmentation techniques," *IEEE/ACM Transactions on Audio, Speech, and Language Processing*, vol. 32, pp. 1214–1225, 2024.
- [21] S. Lutati, E. Nachmani, and L. Wolf, "Separate and diffuse: Using a pretrained diffusion model for better source separation," in *The Twelfth International Conference on Learning Representations*, 2024.
- [22] E. Cohen, H. V. Habi, R. Peretz, and A. Netzer, "Fully quantized neural networks for audio source separation," *IEEE Open Journal of Signal Processing*, pp. 1–9, 2024.
- [23] J. Pons, X. Liu, S. Pascual, and J. Serrà, "GASS: Generalizing audio source separation with large-scale data," in *ICASSP 2024 - 2024 IEEE International Conference on Acoustics, Speech and Signal Processing (ICASSP)*, 2024, pp. 546–550.
- [24] G.-J. Jang and T.-W. Lee, "A maximum likelihood approach to single-channel source separation," *The Journal of Machine Learning Research*, vol. 4, pp. 1365–1392, 2003.
- [25] C. Févotte, N. Bertin, and J.-L. Durrieu, "Nonnegative Matrix Factorization with the Itakura-Saito Divergence: With Application to Music Analysis," *Neural Computation*, vol. 21, no. 3, pp. 793–830, 03 2009.
- [26] J. R. Hershey, Z. Chen, J. Le Roux, and S. Watanabe, "Deep clustering: Discriminative embeddings for segmentation and separation," in *2016 IEEE International Conference on Acoustics, Speech and Signal Processing*, 2016, pp. 31–35.
- [27] C.-H. Lin, C.-Y. Chi, L. Chen, D. J. Miller, and Y. Wang, "Detection of sources in non-negative blind source separation by minimum description length criterion," *IEEE Transactions on Neural Networks and Learning Systems*, vol. 29, no. 9, pp. 4022–4037, 2018.
- [28] L. Drude, D. Hasenklever, and R. Haeb-Umbach, "Unsupervised training of a deep clustering model for multichannel blind source separation," in *IEEE International Conference on Acoustics, Speech and Signal Processing*, 2019, pp. 695–699.
- [29] S. Ke, R. Hu, X. Wang, T. Wu, G. Li, and Z. Wang, "Single channel multi-speaker speech separation based on quantized ratio mask and residual network," *Multimedia Tools and Applications*, vol. 79, no. 43, pp. 32 225–32 241, Nov. 2020.
- [30] H. D. Do, S. T. Tran, and D. T. Chau, "Speech source separation using variational autoencoder and bandpass filter," *IEEE Access*, vol. 8, pp. 156 219–156 231, 2020.
- [31] S. Wisdom, E. Tzinis, H. Erdogan, R. Weiss, K. Wilson, and J. Hershey, "Unsupervised sound separation using mixture invariant training," in *Advances in Neural Information Processing Systems*, vol. 33, 2020, pp. 3846–3857.
- [32] J. Neri, R. Badeau, and P. Depalle, "Unsupervised blind source separation with variational auto-encoders," in *29th European Signal Processing Conference*, 2021, pp. 311–315.
- [33] S. Liu, A. Mallol-Ragolta, E. Parada-Cabaleiro, K. Qian, X. Jing, A. Kathan, B. Hu, and B. W. Schuller, "Audio self-supervised learning: A survey," *Patterns*, vol. 3, no. 12, p. 100616, 2022.
- [34] T. Denton, S. Wisdom, and J. R. Hershey, "Improving bird classification with unsupervised sound separation," in *2022 IEEE International Conference on Acoustics, Speech and Signal Processing*, 2022, pp. 636–640.
- [35] R. Morel, G. Rochette, R. Leonarduzzi, J.-P. Bouchaud, and S. Mallat, "Scale dependencies and self-similar models with wavelet scattering spectra," 2022.
- [36] J. Bruna and S. Mallat, "Invariant scattering convolution networks," *IEEE Transactions on Pattern Analysis and Machine Intelligence*, vol. 35, no. 8, pp. 1872–1886, 2013.
- [37] D. P. Kingma and M. Welling, "Auto-encoding variational Bayes," in *International Conference on Learning Representations*, 2014.
- [38] S. N. B. Paige, J.-W. van de Meent, A. Desmaison, N. Goodman, P. Kohli, F. Wood, and P. Torr, "Learning disentangled representations with semi-supervised deep generative models," in *Advances in Neural Information Processing Systems*, vol. 30, 2017.
- [39] E. Jang, S. Gu, and B. Poole, "Categorical reparameterization with Gumbel-softmax," in *International Conference on Learning Representations*, 2017.
- [40] A. Siahkoohi, R. Morel, M. V. de Hoop, E. Allys, G. Sainton, and T. Kawamura, "Unearthing InSights into Mars: Unsupervised source separation with limited data," in *Proceedings of the 40th International Conference on Machine Learning*, vol. 202, 07 2023, pp. 31 754–31 772.
- [41] D. Giardini, P. Lognonné, W. B. Banerdt, W. T. Pike, U. Christensen, S. Ceylan, J. F. Clinton, M. van Driel, S. C. Stähler, M. Böse *et al.*,

- “The seismicity of Mars,” *Nature Geoscience*, vol. 13, no. 3, pp. 205–212, Mar. 2020.
- [42] M. Golombek, N. Warner, J. Grant, E. Hauber, V. Ansan, C. Weitz, N. Williams, C. Charalambous, S. Wilson, A. DeMott *et al.*, “Geology of the InSight landing site on Mars,” *Nature communications*, vol. 11, no. 1, pp. 1–11, 2020.
- [43] B. Knapmeyer-Endrun and T. Kawamura, “NASA’s InSight mission on Mars—first glimpses of the planet’s interior from seismology,” *Nature Communications*, vol. 11, no. 1, pp. 1–4, 2020.
- [44] A. C. Horleston, J. F. Clinton, S. Ceylan, D. Giardini, C. Charalambous, J. C. E. Irving, P. Lognonné, S. C. Stähler, G. Zenhäusern, N. L. Dahmen, C. Duran, T. Kawamura, A. Khan, D. Kim, M. Plasman, F. Euchner, C. Beghein, E. Beucler, Q. Huang, M. Knapmeyer, B. Knapmeyer-Endrun, V. Lekić, J. Li, C. Perrin, M. Schimmel, N. C. Schmerr, A. E. Stott, E. Stutzmann, N. A. Teanby, Z. Xu, M. Panning, and W. B. Banerdt, “The far side of Mars: Two distant marsquakes detected by InSight,” *The Seismic Record*, vol. 2, no. 2, pp. 88–99, 04 2022.
- [45] S. Ceylan, J. F. Clinton, D. Giardini, S. C. Stähler, N. Horleston, T. Kawamura, M. Böse, C. Charalambous, N. L. Dahmen, M. van Driel, C. Durán, F. Euchner, A. Khan, D. Kim, M. Plasman, J.-R. Scholz, G. Zenhäusern, E. Beucler, R. F. Garcia, S. Kedar, M. Knapmeyer, P. Lognonné, M. P. Panning, C. Perrin, W. T. Pike, A. E. Stott, and W. B. Banerdt, “The marsquake catalogue from InSight, sols 0–1011,” *Physics of the Earth and Planetary Interiors*, vol. 333, p. 106943, 2022.
- [46] M. P. Panning, W. B. Banerdt, C. Beghein, S. Carrasco, S. Ceylan, J. F. Clinton, P. Davis, M. Drilleau, D. Giardini, A. Khan, D. Kim, B. Knapmeyer-Endrun, J. Li, P. Lognonné, S. C. Stähler, and G. Zenhäusern, “Locating the largest event observed on Mars with multi-orbit surface waves,” *Geophysical Research Letters*, vol. 50, no. 1, p. e2022GL101270, 2023.
- [47] InSight Marsquake Service, “Mars seismic catalogue, InSight mission; V14 2023-04-01,” 2023.
- [48] D. Banfield, A. Spiga, C. Newman, F. Forget, M. Lemmon, R. Lorenz, N. Murdoch, D. Viudez-Moreiras, J. Pla-Garcia, R. F. Garcia, P. Lognonné, Ö. Karatekin, C. Perrin, L. Martire, N. Teanby, B. V. Hove, J. N. Maki, B. Kenda, N. T. Mueller, S. Rodríguez, T. Kawamura, J. B. McClean, A. E. Stott, C. Charalambous, E. Millour, C. L. Johnson, A. Mittelholz, A. Määttänen, S. R. Lewis, J. Clinton, S. C. Stähler, S. Ceylan, D. Giardini, T. Warren, W. T. Pike, I. Daubar, M. Golombek, L. Rolland, R. Widmer-Schmidrig, D. Mimoun, É. Beucler, A. Jacob, A. Lucas, M. Baker, V. Ansan, K. Hurst, L. Mora-Sotomayor, S. Navarro, J. Torres, A. Lepinette, A. Molina, M. Marin-Jimenez, J. Gomez-Elvira, V. Peinado, J.-A. Rodriguez-Manfredi, B. T. Carcich, S. Sackett, C. T. Russell, T. Spohn, S. E. Smrekar, and W. B. Banerdt, “The atmosphere of Mars as observed by InSight,” *Nature Geoscience*, vol. 13, no. 3, pp. 190–198, 2020.
- [49] C. Beghein, J. Li, E. Weidner, R. Maguire, J. Wookey, V. Lekić, P. Lognonné, and W. Banerdt, “Crustal anisotropy in the Martian lowlands from surface waves,” *Geophysical Research Letters*, vol. 49, no. 24, p. e2022GL101508, 2022.
- [50] P. Lognonné, W. B. Banerdt, W. Pike, D. Giardini, U. Christensen, R. F. Garcia, T. Kawamura, S. Kedar, B. Knapmeyer-Endrun, L. Margerin *et al.*, “Constraints on the shallow elastic and anelastic structure of mars from insight seismic data,” *Nature Geoscience*, vol. 13, no. 3, pp. 213–220, 2020.
- [51] R. D. Lorenz, A. Spiga, P. Lognonné, M. Plasman, C. E. Newman, and C. Charalambous, “The whirlwinds of Elysium: A catalog and meteorological characteristics of “dust devil” vortices observed by InSight on Mars,” *Icarus*, vol. 355, p. 114119, 2021.
- [52] J. Bruna, S. Mallat, E. Bacry, and J.-F. Muzy, “Intermittent process analysis with scattering moments,” *The Annals of Statistics*, vol. 43, no. 1, pp. 323–351, 2015.
- [53] L. Seydoux, R. Balestrieri, P. Poli, M. d. Hoop, M. Campillo, and R. Baraniuk, “Clustering earthquake signals and background noises in continuous seismic data with unsupervised deep learning,” *Nature communications*, vol. 11, no. 1, p. 3972, Aug. 2020.
- [54] Á. B. Rodríguez, R. Balestrieri, S. De Angelis, M. C. Benítez, L. Zuccarello, R. Baraniuk, J. M. Ibáñez, and V. Maarten, “Recurrent scattering network detects metastable behavior in polyphonic seismo-volcanic signals for volcano eruption forecasting,” *IEEE Transactions on Geoscience and Remote Sensing*, vol. 60, pp. 1–23, 2021.
- [55] G. Wornell, “Wavelet-based representations for the $1/f$ family of fractal processes,” *Proceedings of the IEEE*, vol. 81, no. 10, pp. 1428–1450, 1993.
- [56] L. Gatys, A. S. Ecker, and M. Bethge, “Texture synthesis using convolutional neural networks,” in *Advances in Neural Information Processing Systems*, vol. 28, 2015.
- [57] M. I. Jordan, Z. Ghahramani, T. S. Jaakkola, and L. K. Saul, “An introduction to variational methods for graphical models,” *Machine Learning*, vol. 37, no. 2, pp. 183–233, 1999.
- [58] D. M. Blei, A. Kucukelbir, and J. D. McAuliffe, “Variational inference: A review for statisticians,” *Journal of the American statistical Association*, vol. 112, no. 518, pp. 859–877, 2017.
- [59] B. Regalado-Saint Blancard, E. Allys, F. Boulanger, F. Levrier, and N. Jeffrey, “A new approach for the statistical denoising of Planck interstellar dust polarization data,” *Astronomy & Astrophysics*, vol. 649, p. L18, 2021.
- [60] Delouis, J.-M., Allys, E., Gauvrit, E., and Boulanger, F., “Non-Gaussian modelling and statistical denoising of Planck dust polarisation full-sky maps using scattering transforms,” *Astronomy & Astrophysics*, vol. 668, p. A122, 2022.
- [61] J.-R. Scholz, R. Widmer-Schmidrig, P. Davis, P. Lognonné, B. Pinot, R. F. Garcia, K. Hurst, L. Pou, F. Nimmo, S. Barkaoui, S. de Raucourt, B. Knapmeyer-Endrun, M. Knapmeyer, G. Orhand-Mainsant, N. Compaire, A. Cuvier, E. Beucler, M. Bonnin, R. Joshi, G. Sainont, E. Stutzmann, M. Schimmel, A. Horleston, M. Böse, S. Ceylan, J. Clinton, M. van Driel, T. Kawamura, A. Khan, S. C. Stähler, D. Giardini, C. Charalambous, A. E. Stott, W. T. Pike, U. R. Christensen, and W. B. Banerdt, “Detection, analysis, and removal of glitches from InSight’s seismic data from Mars,” *Earth and Space Science*, vol. 7, no. 11, p. e2020EA001317, 2020.
- [62] S. C. Stähler, A. Mittelholz, C. Perrin, T. Kawamura, D. Kim, M. Knapmeyer, G. Zenhäusern, J. Clinton, D. Giardini, P. Lognonné, and W. B. Banerdt, “Tectonics of Cerberus Fossae unveiled by marsquakes,” *Nature Astronomy*, vol. 6, no. 12, pp. 1376–1386, Dec. 2022.
- [63] InSight Mars SEIS Data Service, “SEIS raw data, Insight Mission,” IPGP, JPL, CNES, ETHZ, ICL, MPS, ISAE-Supaero, LPG, MFSC, 2019. [Online]. Available: [10.18715/SEIS.INSIGHT.XB_2016](https://doi.org/10.18715/SEIS.INSIGHT.XB_2016)
- [64] S. Barkaoui, P. Lognonné, T. Kawamura, É. Stutzmann, L. Seydoux, V. Maarten, R. Balestrieri, J.-R. Scholz, G. Sainont, M. Plasman *et al.*, “Anatomy of continuous Mars SEIS and pressure data from unsupervised learning,” *Bulletin of the Seismological Society of America*, vol. 111, no. 6, pp. 2964–2981, 2021.
- [65] D. P. Kingma and J. Ba, “Adam: A method for stochastic optimization,” 2014.
- [66] A. Chatain, A. Spiga, D. Banfield, F. Forget, and N. Murdoch, “Seasonal variability of the daytime and nighttime atmospheric turbulence experienced by InSight on Mars,” *Geophysical Research Letters*, vol. 48, no. 22, p. e2021GL095453, 2021.
- [67] F. Ferri, P. H. Smith, M. Lemmon, and N. O. Rennó, “Dust devils as observed by Mars Pathfinder,” *Journal of Geophysical Research: Planets*, vol. 108, no. E12, 2003.
- [68] L. McInnes, J. Healy, N. Saul, and L. Großberger, “UMAP: Uniform manifold approximation and projection,” *Journal of Open Source Software*, vol. 3, no. 29, p. 861, 2018.
- [69] R. Balestrieri, R. Cosentino, H. Glotin, and R. Baraniuk, “Spline filters for end-to-end deep learning,” in *Proceedings of the 35th International Conference on Machine Learning*, vol. 80, Jul. 2018, pp. 364–373.
- [70] B. Knapmeyer-Endrun, M. P. Panning, F. Bissig, R. Joshi, A. Khan, D. Kim, V. Lekić, B. Tausin, S. Tharimena, M. Plasman, N. Compaire, R. F. Garcia, L. Margerin, M. Schimmel, Éléonore Stutzmann, N. Schmerr, E. Bozdağ, A.-C. Plesa, M. A. Wiczorek, A. Broquet, D. Antonangeli, S. M. McLennan, H. Samuel, C. Michaut, L. Pan, S. E. Smrekar, C. L. Johnson, N. Brinkman, A. Mittelholz, A. Rivoldini, P. M. Davis, P. Lognonné, B. Pinot, J.-R. Scholz, S. Stähler, M. G. Knapmeyer, M. van Driel, D. Giardini, and W. B. Banerdt, “Thickness and structure of the martian crust from InSight seismic data,” *Science*, vol. 373, no. 6553, pp. 438–443, 2021.
- [71] S. C. Stähler, A. Khan, W. B. Banerdt, P. Lognonné, D. Giardini, S. Ceylan, M. Drilleau, A. C. Duran, R. F. Garcia, Q. Huang, D. Kim, V. Lekic, H. Samuel, M. Schimmel, N. Schmerr, D. Sollberger, Éléonore Stutzmann, Z. Xu, D. Antonangeli, C. Charalambous, P. M. Davis, J. C. E. Irving, T. Kawamura, M. Knapmeyer, R. Maguire, A. G. Marusiak, M. P. Panning, C. Perrin, A.-C. Plesa, A. Rivoldini, C. Schmelzbach, G. Zenhäusern, Éric Beucler, J. Clinton, N. Dahmen, M. van Driel, T. Gudkova, A. Horleston, W. T. Pike, M. Plasman, and S. E. Smrekar, “Seismic detection of the martian core,” *Science*, vol. 373, no. 6553, pp. 443–448, 2021.
- [72] E. Bacry, J. Delour, and J. F. Muzy, “Multifractal random walk,” *Physical Review E*, vol. 64, p. 026103, Jul. 2001.
- [73] O. Chanal, B. Chabaud, B. Castaing, and B. Hébral, “Intermittency in a turbulent low temperature gaseous helium jet,” *The European Physical Journal B - Condensed Matter and Complex Systems*, vol. 17, no. 2, pp. 309–317, Sep. 2000.

APPENDIX A

ALL IDENTIFIED CLUSTERS AND THEIR REPRESENTATIVE WAVEFORMS

In this section, we present the complete set of nine clusters identified by the fVAE across four different time scales. Figs. 8, 10, 12 and 14 display the occurrence time histograms of these clusters for 51.2-second timescale, 3.4-minute timescale, 13.6-minute timescale, and 54.6-minute timescale, respectively, by aggregating data from the entire mission. Additionally, we provide the representative aligned waveforms for each cluster at all time scales. Figs. 9, 11, 13 and 15 depict these waveforms for 51.2-second timescale, 3.4-minute timescale, 13.6-minute timescale, and 54.6-minute timescale, respectively.

In a similar study, [64] also aimed at detecting and clustering microevents and noise patterns in the seismic data recorded during the InSight mission on Mars. The authors identified nine main clusters of events and noise patterns in the seismic data when focusing on 100 s time windows. Similar to our observations with the finest timescale used in our results, [64] mostly identified transient events, such as pressure drops and various types of glitches. Since their timescale was slightly longer than our finest timescale, they also discovered repeating sequences of glitches with relatively constant time offsets. This is analogous to the two clusters we identify in the 3.4-minute timescale presented in Figs. 11a and 11f, whose time histograms also align with the typical occurrence time of glitches (see Figs. 10a and 10f). Regarding pressure drops, [64] reported that these were mainly spread across three clusters. Although the aligned waveforms of clusters 0, 7, and 8 identified by our approach (see Figs. 9a, 9h and 9i) do not indicate pressure drops, the latent space visualization of pressure drops from the catalog at the finest scale (see Fig. 7b) shows that these pressure drops are mostly concentrated in cluster 7, with the rest primarily in clusters 0 and 8. Additionally, [64] characterized daily and seasonal variations in event occurrence related to temperature changes, which we similarly observed in Fig. 4.

Beyond these observations, our multi-scale approach and the use of scattering spectra, which are more capable at distinguishing between different non-Gaussian stochastic processes than scattering coefficients [35], allowed us to identify more patterns in the datasets, including events with much longer timescales, such as atmospheric-surface interactions due to wind. Furthermore, we utilized the entire seismic dataset to train our model, in contrast to the approximately one week of data used in [64], providing a more comprehensive overview of Martian seismic activity and arguably a more robust data representation. This enriched representation and the multi-scale nature of our approach facilitated the localization of rare marsquakes in the latent space. As noted in [64], due to their rarity, marsquakes do not significantly influence the clustering results. Finally, thanks to our probabilistic multi-scale clustering, we were able to use the scattering spectra representation of signals of interest to perform source separation.

APPENDIX B

FVAE DECODER RECONSTRUCTION QUALITY

In this section, we present the reconstructed input scattering spectra through the fVAE. Figs. 16 to 19 summarize the results for 51.2-second timescale, 3.4-minute timescale, 13.6-minute timescale, and 54.6-minute timescale, respectively. Each one of these figures shows the input scattering spectra (in black) and the corresponding reconstructed input (in red) for the U, V, and W components of four randomly selected waveforms.

APPENDIX C

UNSUPERVISED SEPARATION OF MARSQUAKES

In this section, we showcase the ability of our method to separate signals that, due to their scarcity, do not have a dedicated cluster within the fVAE latent space, e.g., marsquakes (cf. Fig. 7g). Marsquakes are of significant importance as they provide useful information regarding the Mars subsurface, enabling the study of Mars’ interior [70], [71]. Here we apply our proposed unsupervised source separation approach to isolate background noise and transient atmospheric signals from a marsquake recorded on February 3, 2022 [47], which would allow for more accurate downstream study of marsquakes. To achieve this, we select 80 time windows from each cluster in the finest timescale except clusters one and eight, which are concentrated during the day (cf. Figs. 9b and 9i). The reason for this particular choice is threefold: (i) the marsquake (cf. Fig. 20a) is recorded during night Martian time, so having data from the night allows for a better capture of the background signal statistics; (ii) as marsquakes are scarce and do not have a dedicated cluster, the chance of obtaining a time window that is a likely sample from a cluster being a marsquake is slim, reducing the chances of accidentally separating marsquake signals as background noise; and (iii) we found performing source separation at the finest scale allows for better separation of glitches, as they are also short and transient signals.

Next, we use these time windows as representative samples from the background noise (s_i in the context of (10)) with the goal of separating the clean marsquake signal. We solve the optimization problem in (10) with 1000 L-BFGS iterations. The results are depicted in Fig. 20. There are clearly three glitches that we have successfully separated, along with the background noise. Through this example, we demonstrated the effectiveness of our multi-scale source separation method—based on prior information obtained from the fVAE—when the source (the marsquake in this case) is not a prominent source in the entire dataset, i.e., it is an outlier.

APPENDIX D

STYLIZED EXAMPLE

We present a multi-scale synthetic dataset (see Fig. 21) used to validate our model using ground truth sources. We first describe how the dataset is constructed and then we present the results of our clustering and source separation algorithm when applied to this dataset.

A. Synthetic multi-scale dataset

This dataset is composed of events with three distinct timescales w that are outlined below:

- **Large scale** ($w = 2^{12}$). In this timescale, the signal alternates between two different noises to mimic the change in background noise due to day-night periodicity. The first noise is a white noise $\mathbf{x}_1(t)$ and the second one is a multifractal random noise $\mathbf{x}_2(t)$ which is a non-Gaussian noise with intermittency [72]. The large-scale signal is then $\mathbf{x}_{\text{large}}(t) = (1 - \theta(t))\mathbf{x}_1(t) + \theta(t)\mathbf{x}_2(t)$ where $\theta(t)$ is equal to 0 on $[0, w]$ and 1 on $[w + \eta, 2w - \eta]$ for small η , is $2w$ -periodic and has a smooth junction at $t = w$ and at $t = 2w$.
- **Medium scale** ($w = 2^{10}$). This timescale exhibits a single type of events which is a turbulent jet recorded in experimental conditions [73]. Each event has a duration $w = 2^{10}$ and is placed randomly without overlapping, with as many events as the number of “days” defined at large scale.
- **Fine scales** ($w = 2^8$). The signal in this timescale is a mixture of two types of transient events with exponential decay. First one $\mathbf{x}_3(t) = e^{-|t|}$ is symmetrical in $t = 0$, second one $\mathbf{x}_4(t) = e^{-t}\mathbf{1}_{t \geq 0}$ is asymmetrical. Each of these signals is randomly positioned in the time-series with four times more occurrence than the number of “days” in our dataset.

The resulting dataset is a long time-series $\mathbf{x} = \mathbf{x}_{\text{large}} + \mathbf{x}_{\text{medium}} + \mathbf{x}_{\text{fine}}$.

B. Synthetic data clustering

While we are aware of the underlying sources that create this data, we choose to make an uninformed decision in regards to the number of clusters per scale to mimic a more realistic setting. To this end, we use the same architecture and same hyperparameters as the fVAE trained in the context of clustering and source separation data from Mars, with the distinction that we chose our timescales for scattering covariance generation based on the duration of sources in our multi-scale dataset.

Fig. 22 summarizes the identified clusters after training the fVAE. We can indeed identify different patterns at each timescale, some of which clearly indicate the multi-scale sources that were used to generate the data. A portion of the clusters are also comprised of at least two of this sources in combination.

C. Synthetic data source separation

Similar to the case with data from Mars, we can identify certain patterns in the obtained clusters and use another cluster as prior information in order to perform per-cluster source separation. Here we exemplify this by separating the medium-scale source that we added from cluster seven in in the largest scale (pink waveforms in Fig. 24). To achieve this, we select the pink cluster in Fig. 23 as prior cluster as it contains similar background noise to the target cluster but without the medium-scale source. The results of this source separation is shown in

Fig. 25 for three waveforms. According to the results, our approach has been able to successfully identify and separated the medium-scale source from a set of target waveforms with minimal distortion to the other sources.

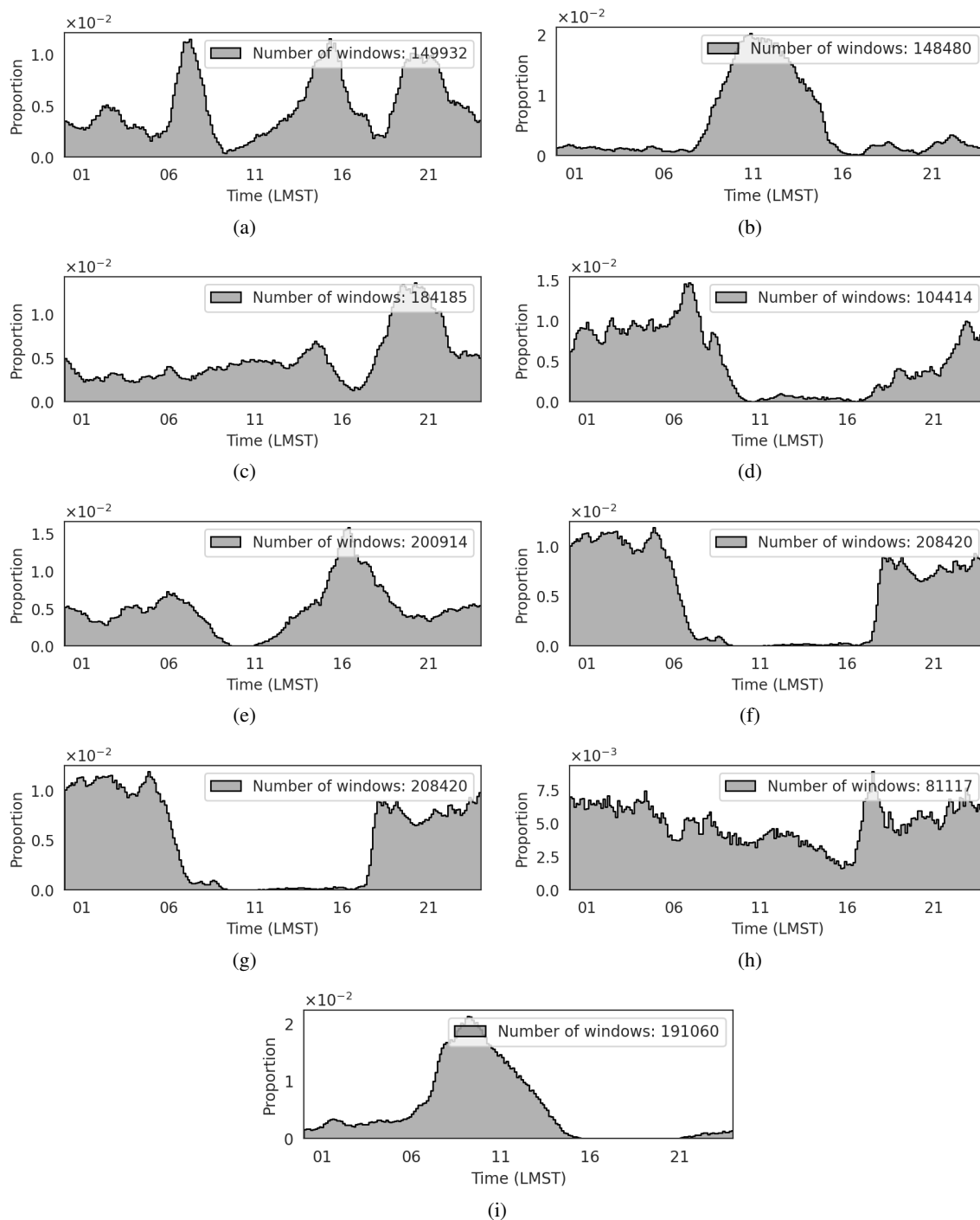


Fig. 8. The occurrence time histogram of all nine identified clusters within the 51.2-second timescale. The horizontal axis of the histograms represents the local mean solar time (LMST). Clusters 0–9 are shown in Figs. 8a to 8i, respectively.

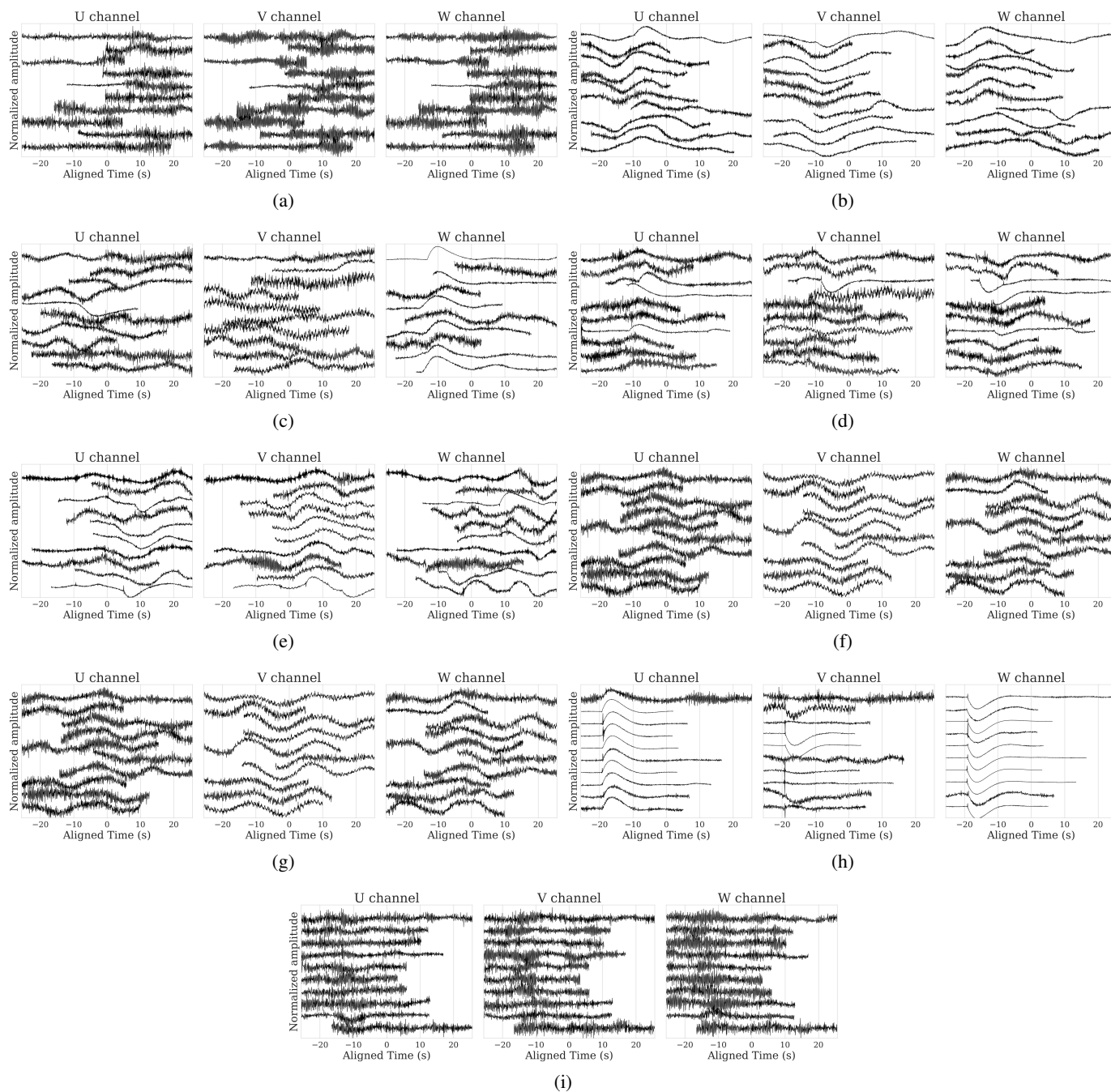


Fig. 9. The aligned waveforms of all nine identified clusters within the 51.2-second timescale. Clusters 0–9 are shown in Figs. 9a to 9i, respectively.

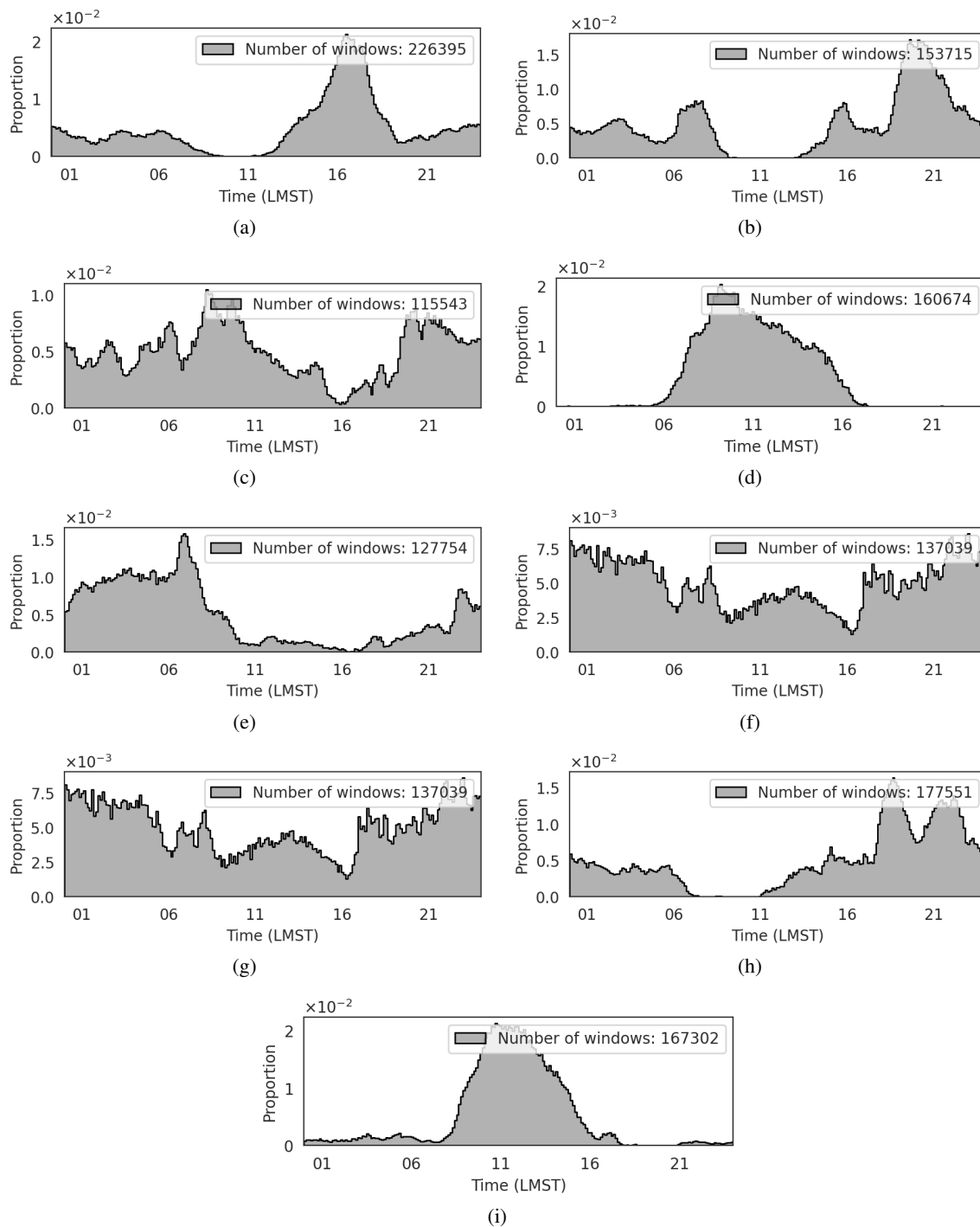


Fig. 10. The occurrence time histogram of all nine identified clusters within the 3.4-minute timescale. The horizontal axis of the histograms represents the local mean solar time (LMST). Clusters 0–9 are shown in Figs. 10a to 10i, respectively.

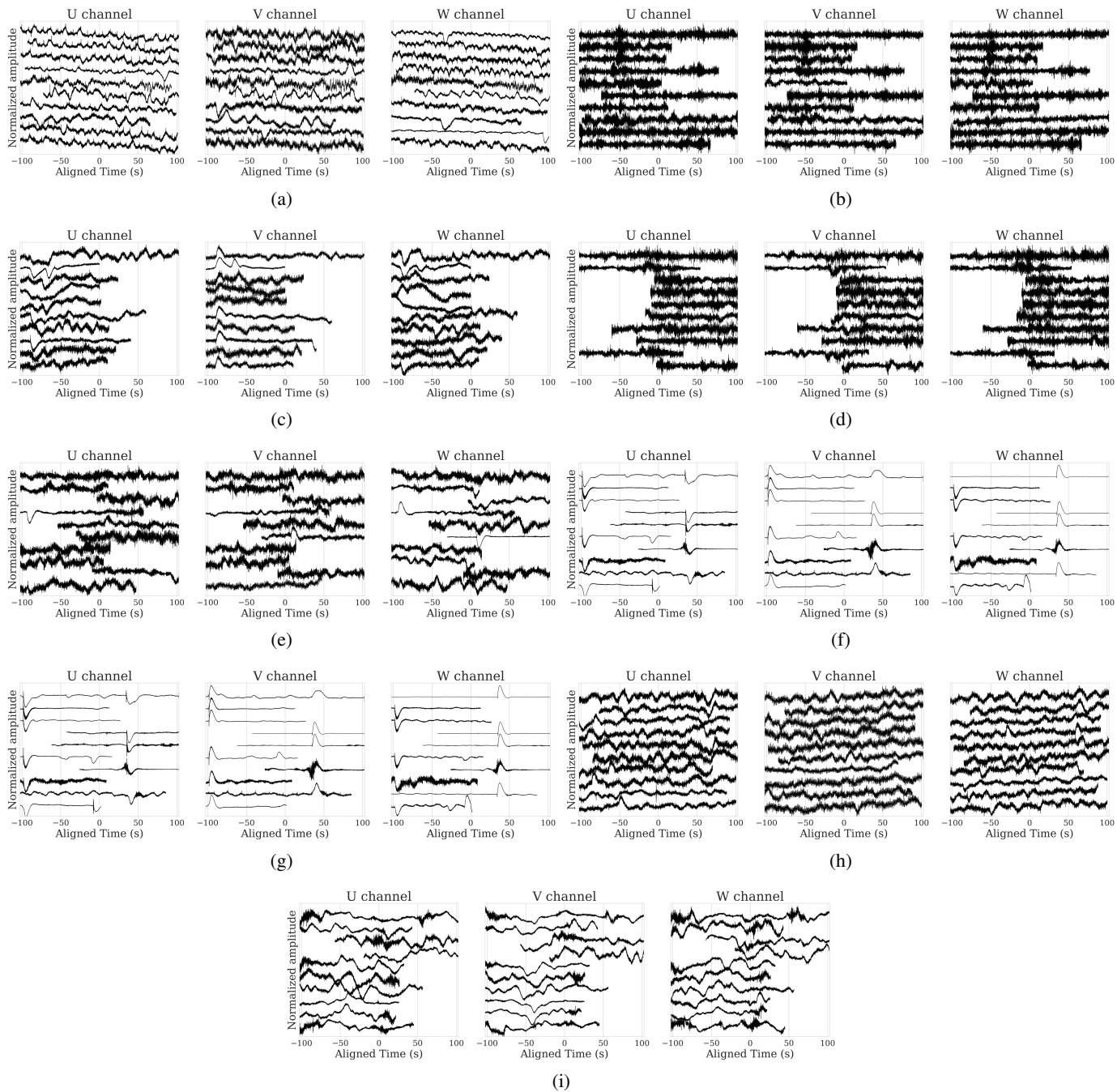


Fig. 11. The aligned waveforms of all nine identified clusters within the 3.4-minute timescale. Clusters 0–9 are shown in Figs. 11a to 11i, respectively.

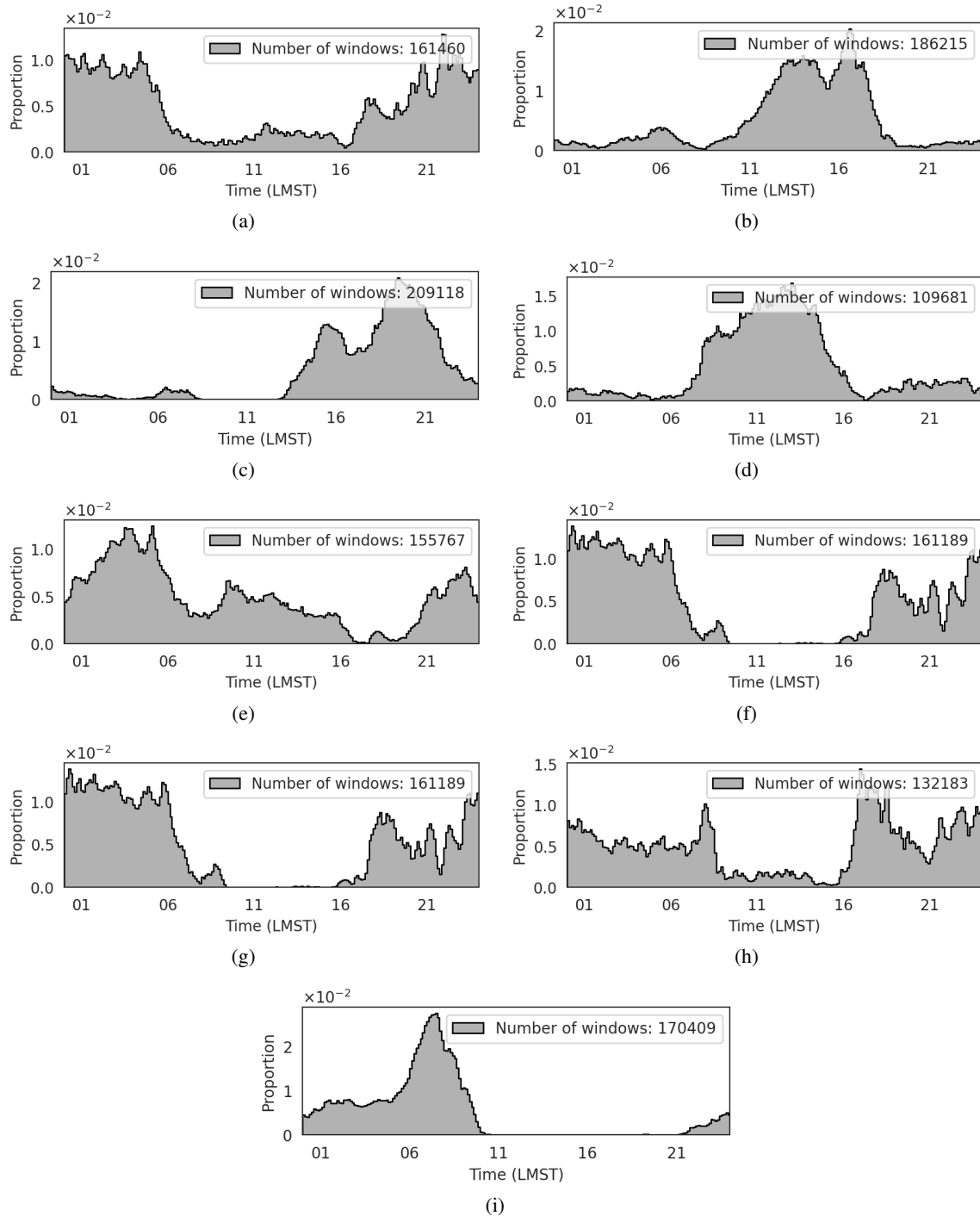


Fig. 12. The occurrence time histogram of all nine identified clusters within the 13.6-minute timescale. The horizontal axis of the histograms represents the local mean solar time (LMST). Clusters 0–9 are shown in Figs. 12a to 12i, respectively.



Fig. 13. The aligned waveforms of all nine identified clusters within the 13.6-minute timescale. Clusters 0–9 are shown in Figs. 13a to 13i, respectively.

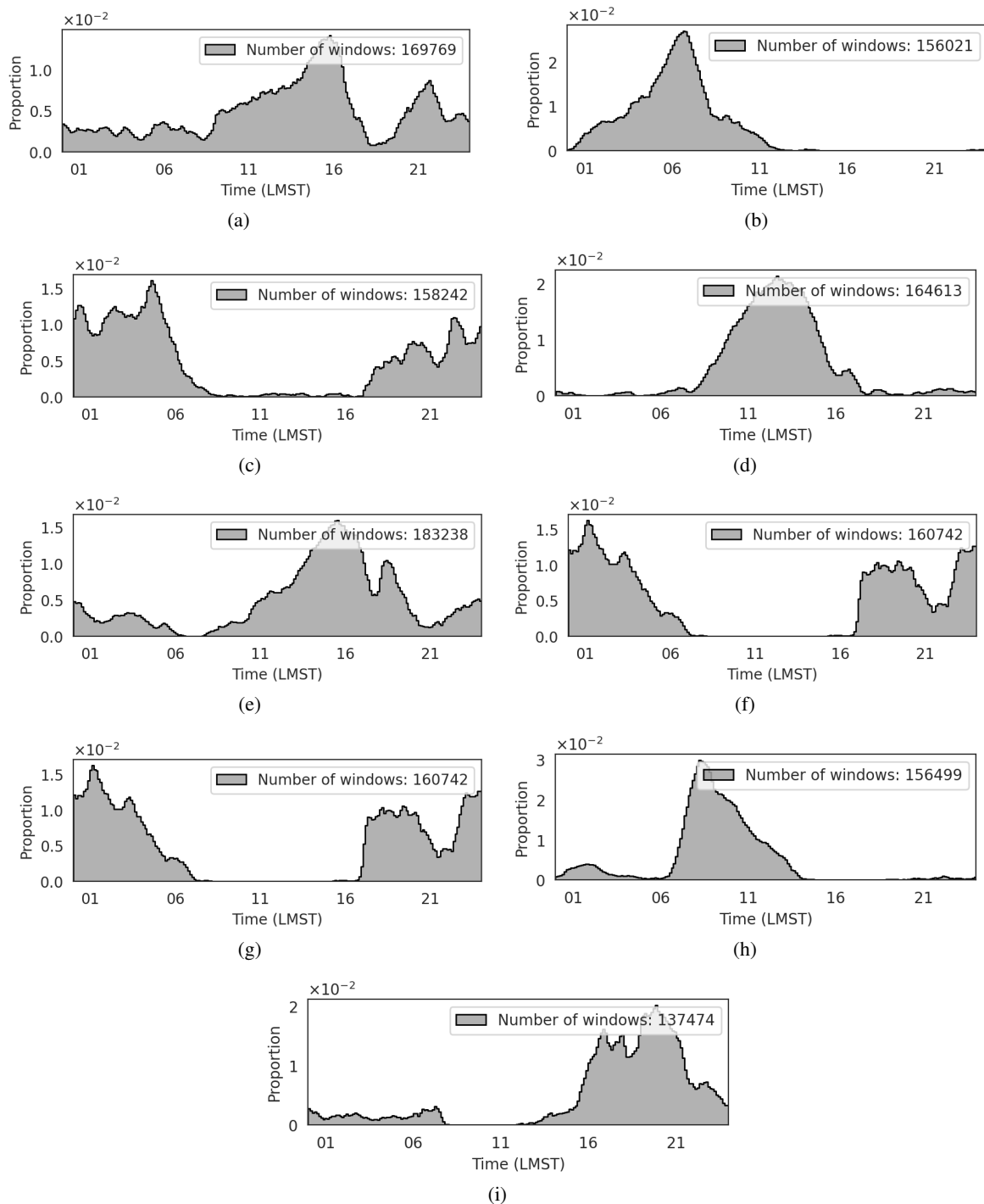


Fig. 14. The occurrence time histogram of all nine identified clusters within the 54.6-minute timescale. The horizontal axis of the histograms represents the local mean solar time (LMST). Clusters 0–9 are shown in Figs. 14a to 14i, respectively.

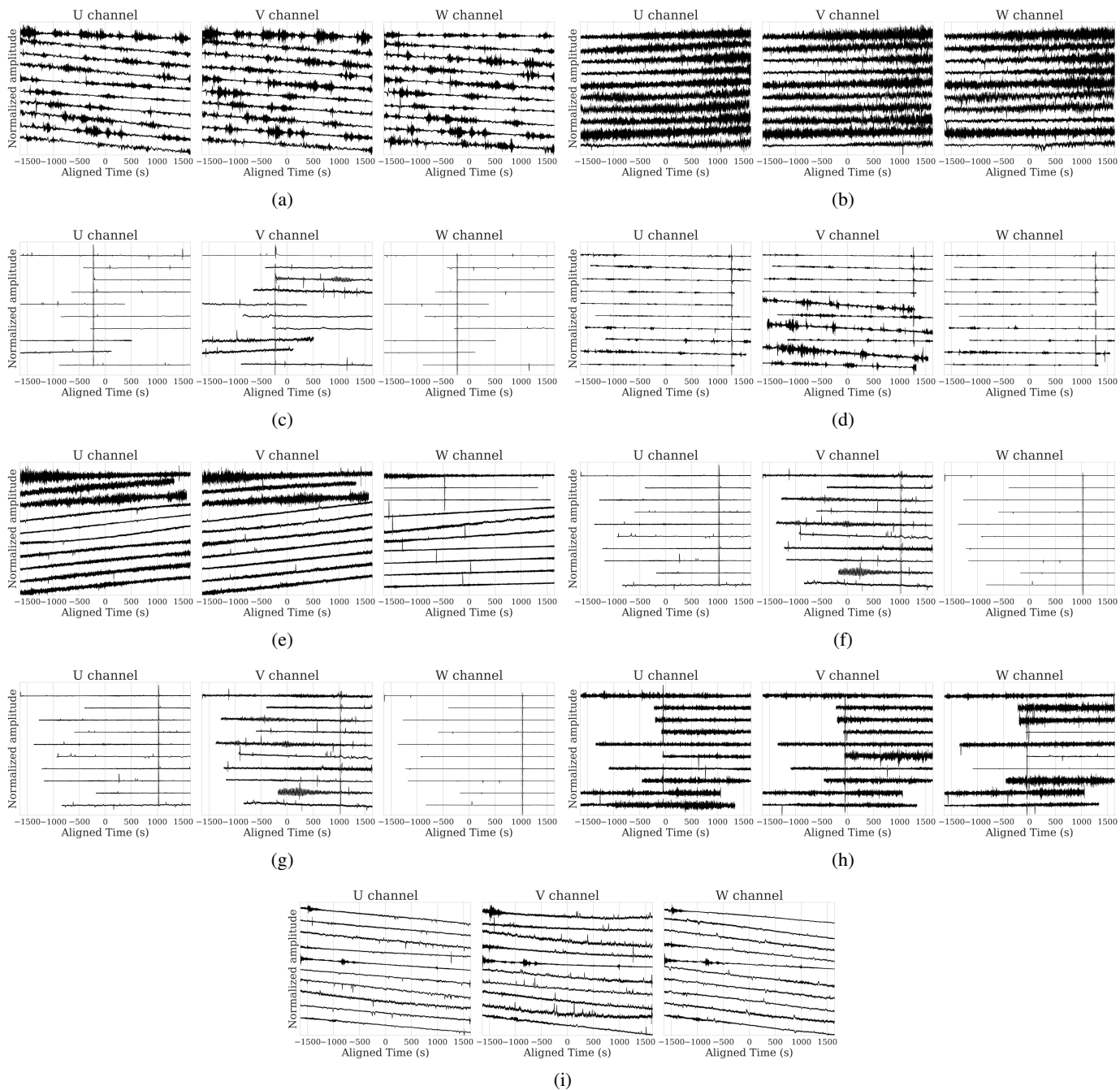


Fig. 15. The aligned waveforms of all nine identified clusters within the 54.6-minute timescale. Clusters 0–9 are shown in Figs. 15a to 15i, respectively.

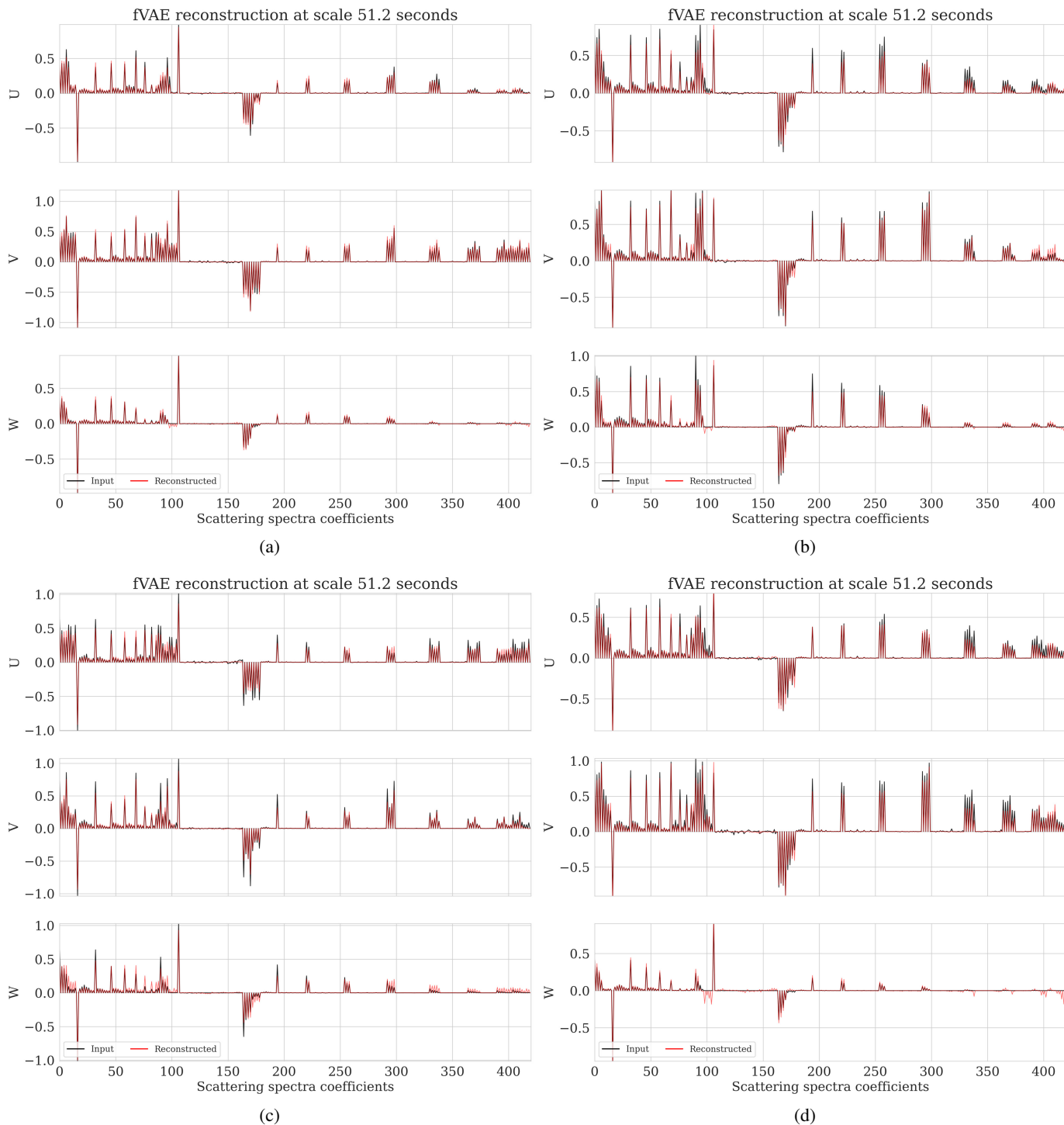


Fig. 16. The input scattering spectra (black) and reconstruction via the fVAE decoder (red) for the U, V, and W components of four random windows from the 51.2-second timescale.

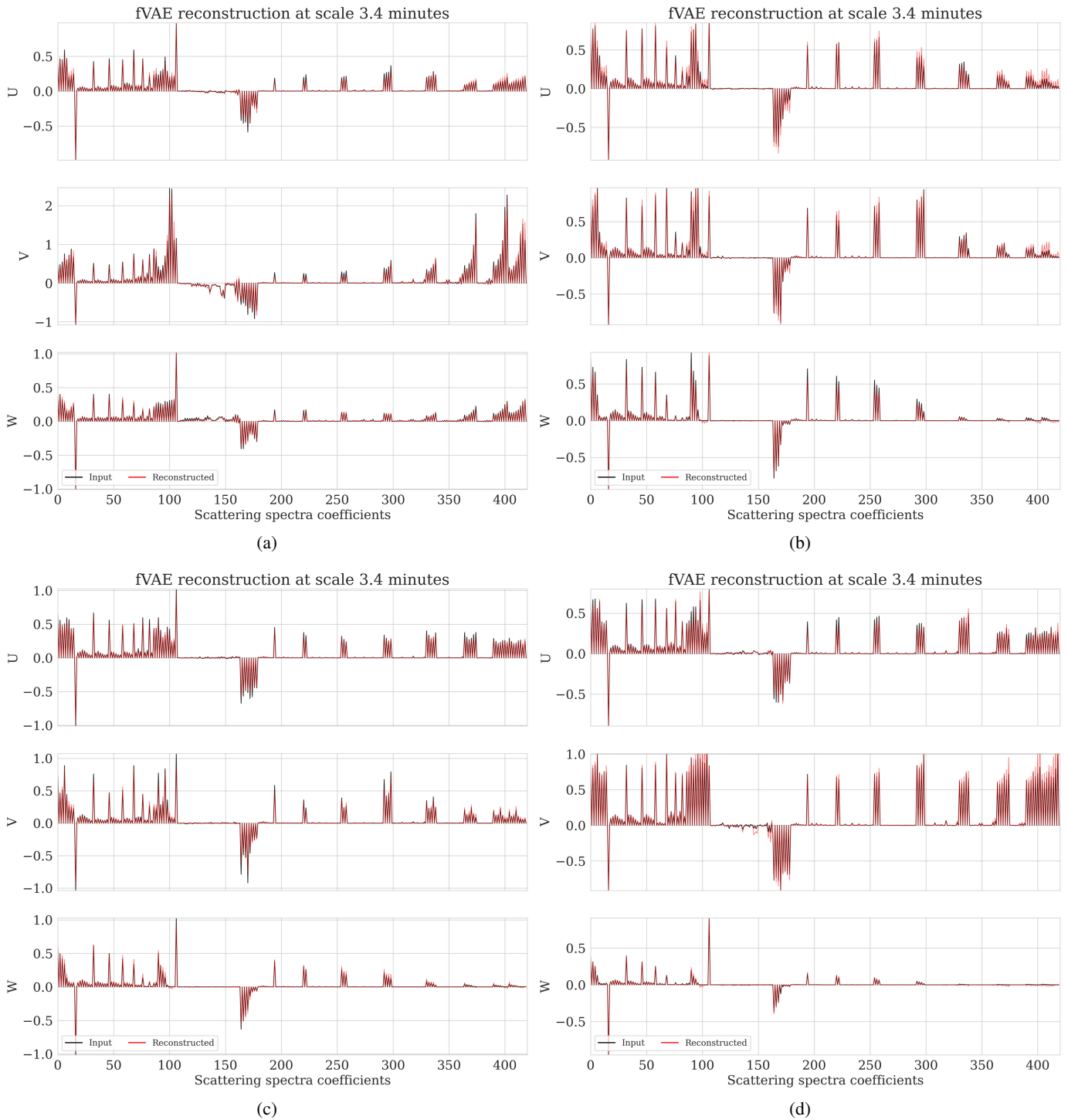


Fig. 17. The input scattering spectra (black) and reconstruction via the fVAE decoder (red) for the U, V, and W components of four random windows from the 3.4-minute timescale.

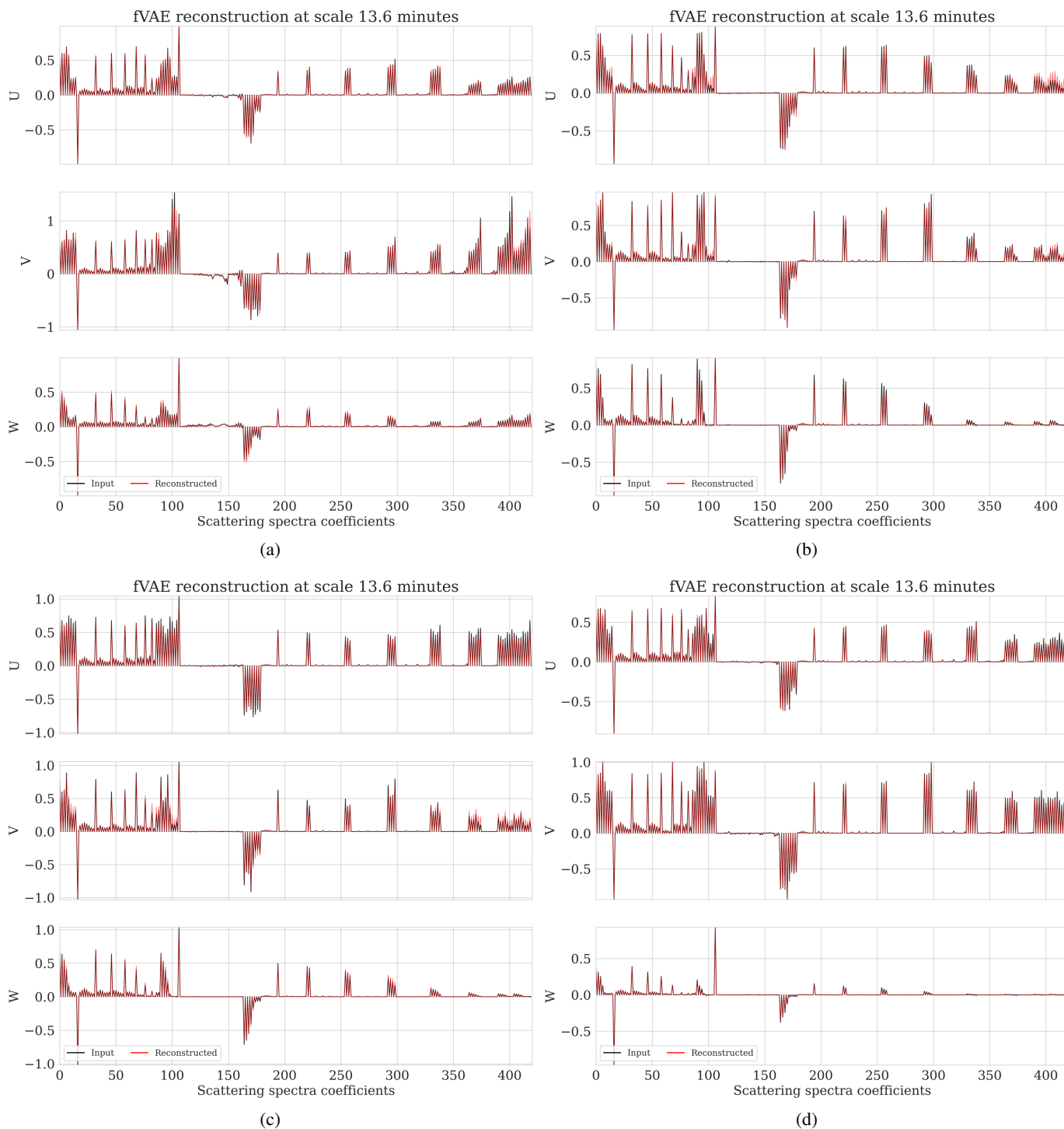


Fig. 18. The input scattering spectra (black) and reconstruction via the fVAE decoder (red) for the U, V, and W components of four random windows from the 13.6-minute timescale.

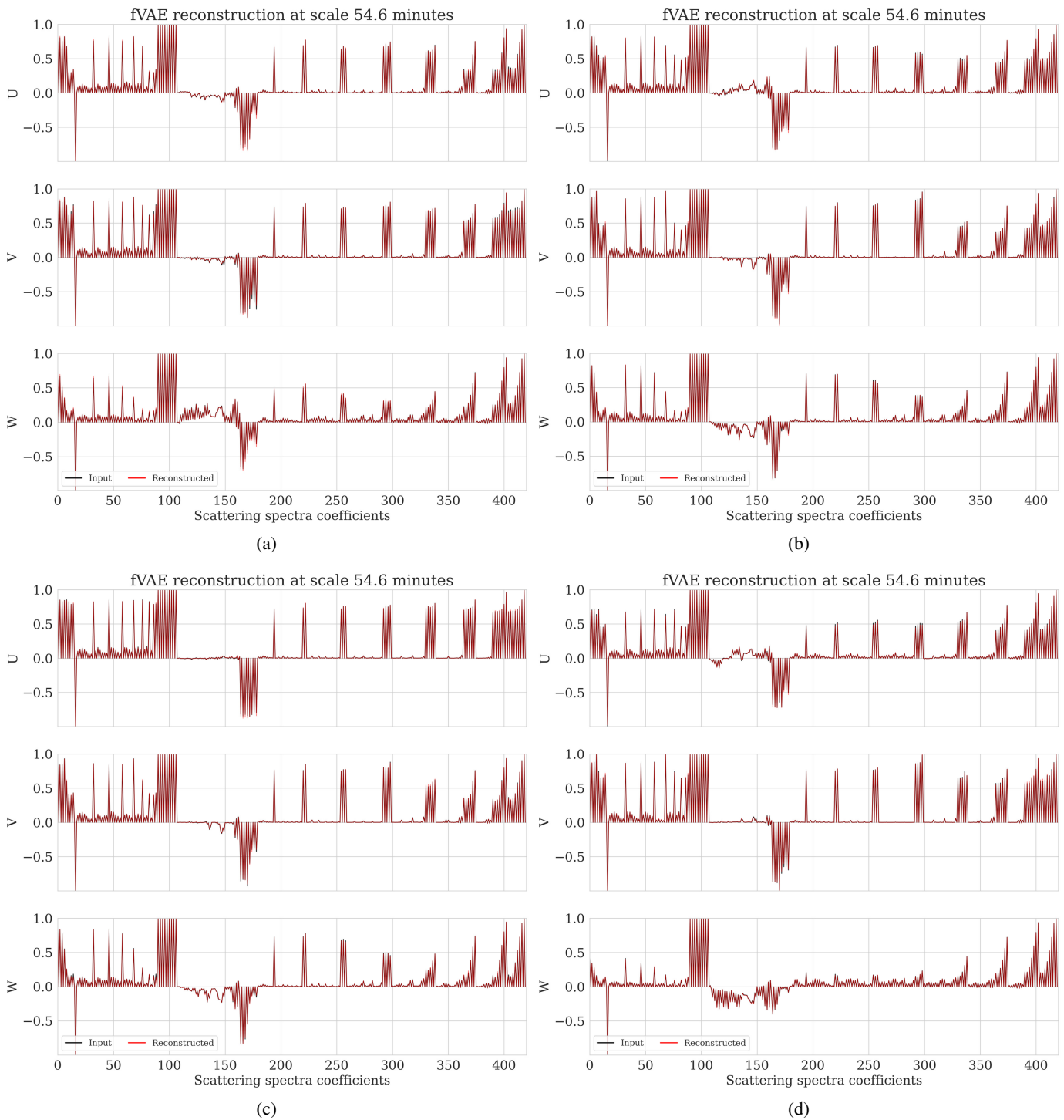


Fig. 19. The input scattering spectra (black) and reconstruction via the fVAE decoder (red) for the U, V, and W components of four random windows from the 54.6-minute timescale.

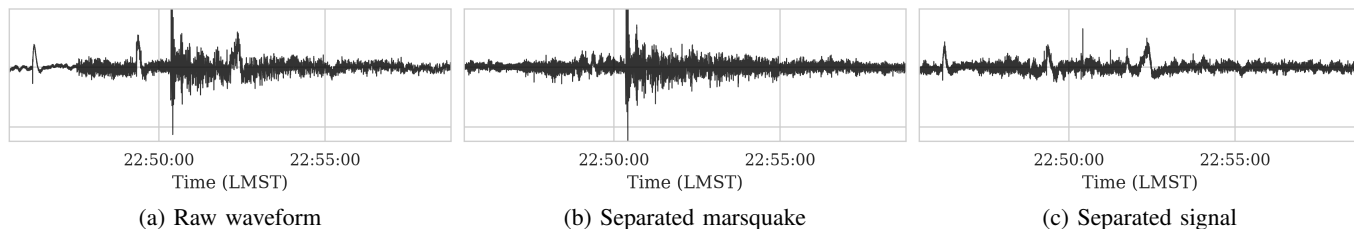


Fig. 20. Unsupervised separation of background noise, including transient atmospheric signals (glitches), from a marsquake (Fig. 20a) recorded by the InSight lander’s seismometer on February 3, 2022 [47]. Approximately eight hours of raw data from the U component were utilized for background noise separation without any explicit prior knowledge of marsquakes or glitches. The separated marsquake is shown Fig. 20b, and the separated signal in shown in Fig. 20c. The horizontal axis of the histograms represents the local mean solar time (LMST).

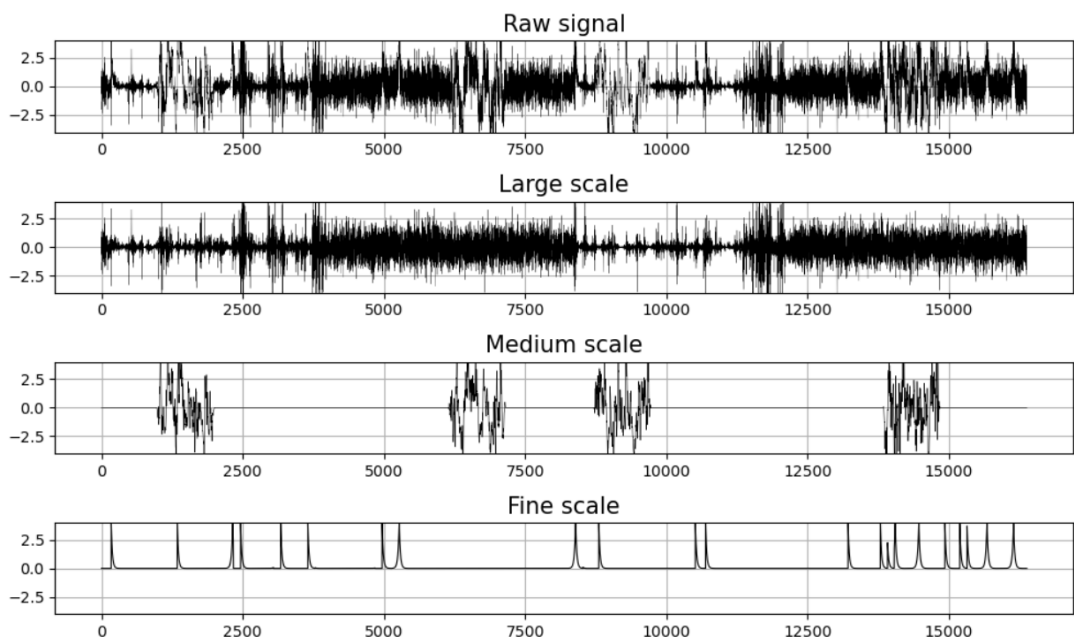


Fig. 21. Synthetic multi-scale dataset.

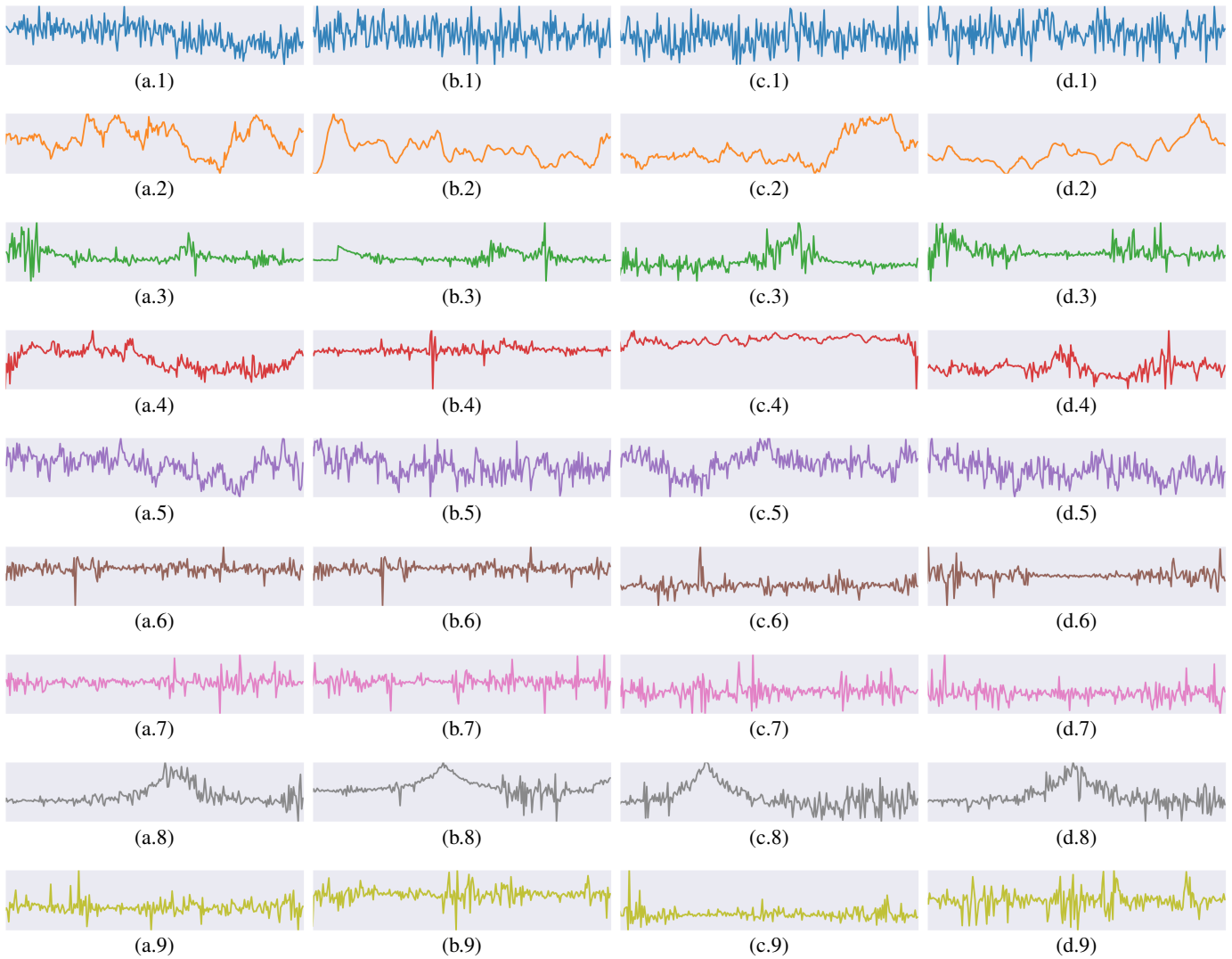


Fig. 22. Waveforms in timescale of 256 sample, with each row from top to bottom illustrating four waveforms corresponding to clusters one to nine in this timescale, respectively.

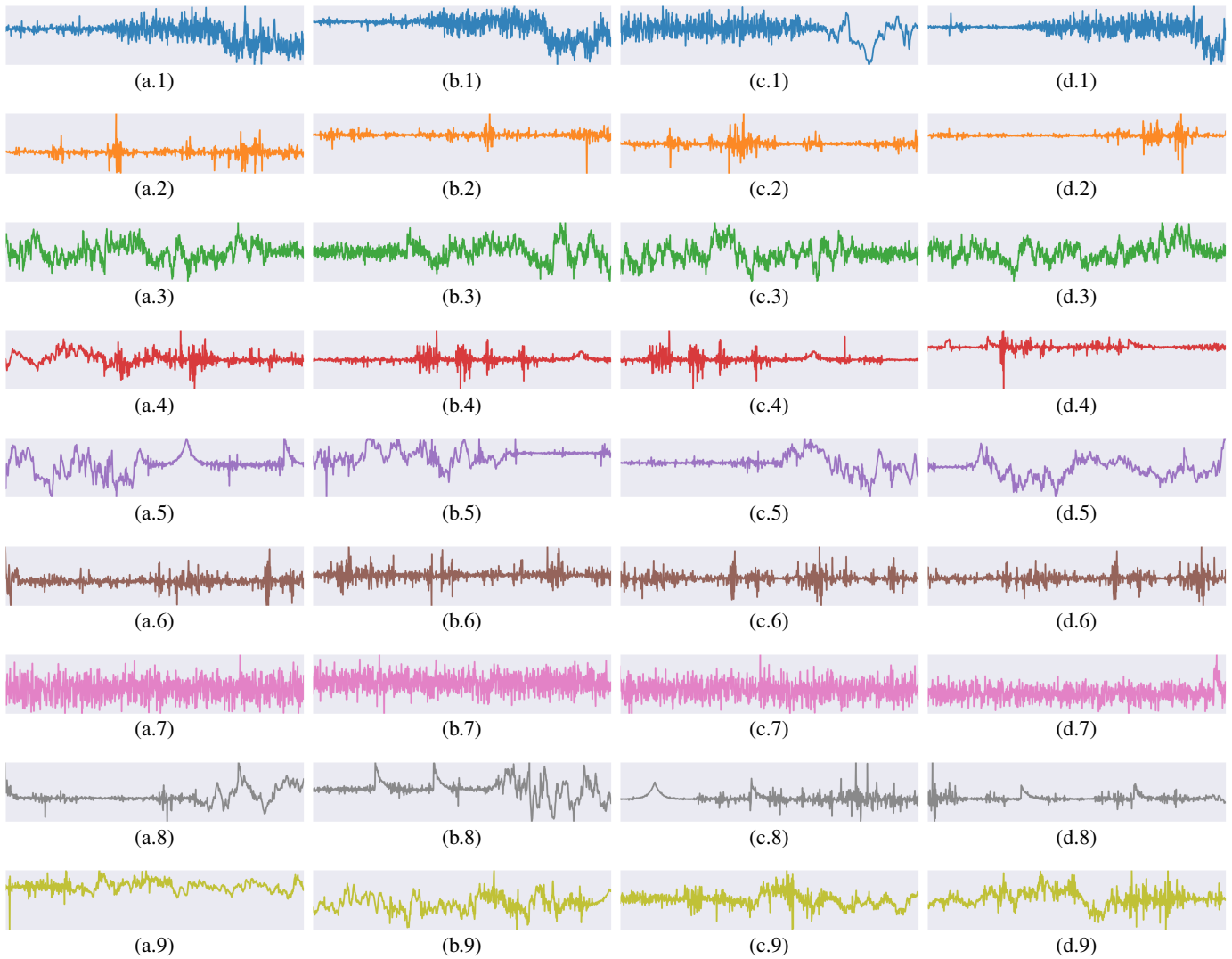


Fig. 23. Waveforms in timescale of 1024 sample, with each row from top to bottom illustrating four waveforms corresponding to clusters one to nine in this timescale, respectively.

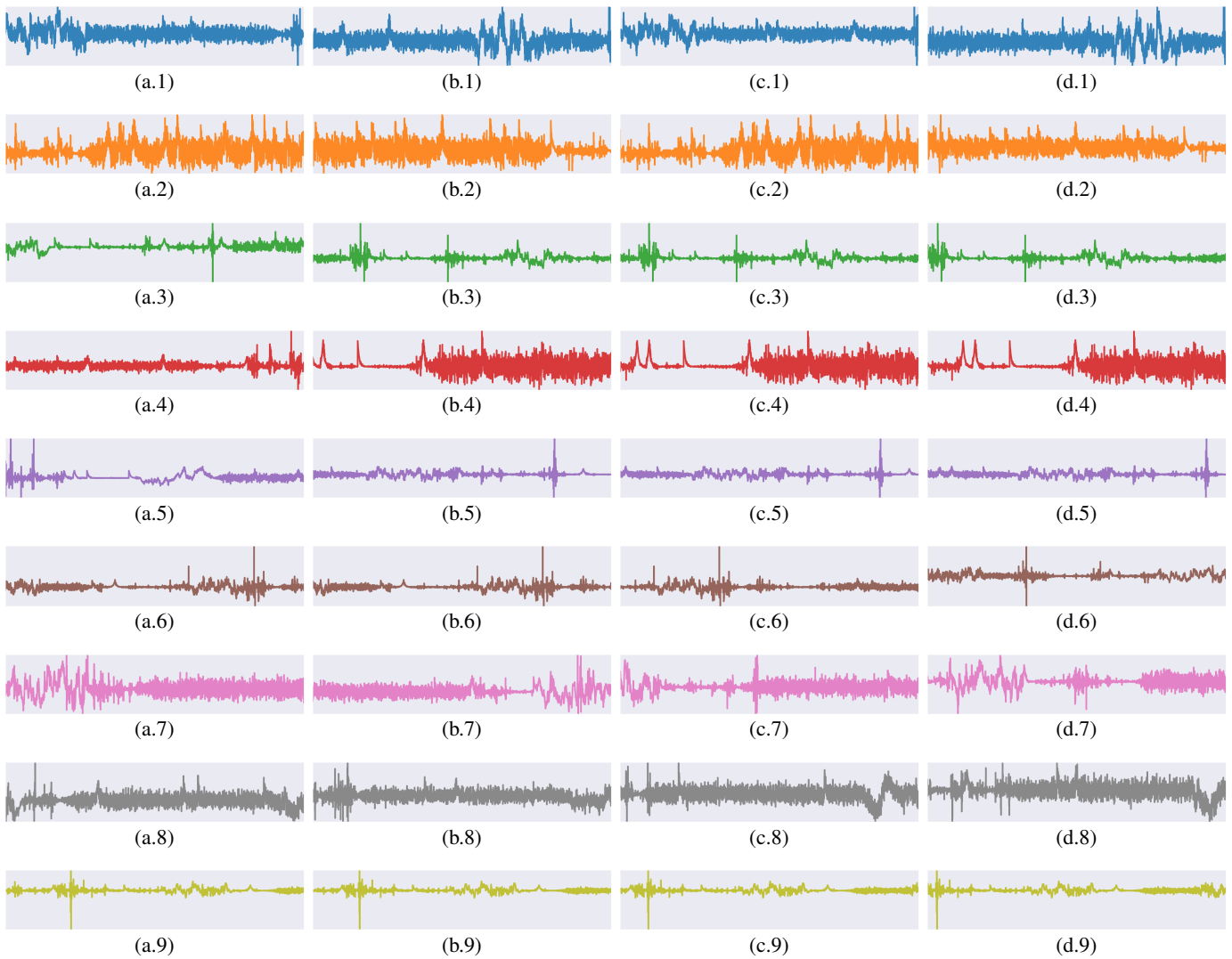


Fig. 24. Waveforms in timescale of 4096 sample, with each row from top to bottom illustrating four waveforms corresponding to clusters one to nine in this timescale, respectively.

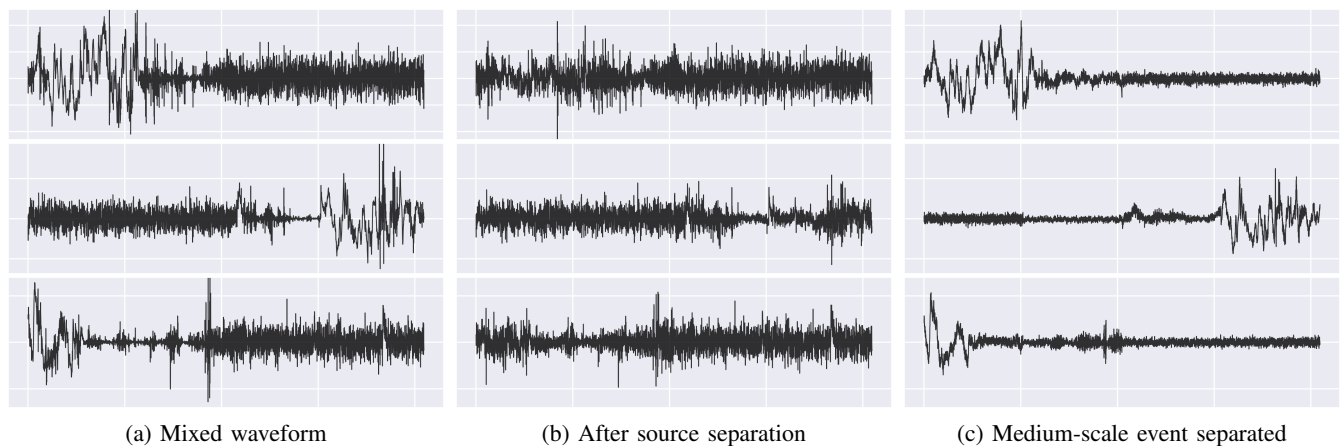


Fig. 25. Removing the medium-scale source.